Dissertação de Mestrado

Inatel
Instituto Nacional de Telecomunicações

GFDM as a Framework for FBMC-OQAM: Iterative Detection and Performance Evaluation

Ivo Bizon Franco de Almeida

Dezembro/2018

Instituto Nacional de Telecomunicações – INATEL

Master's degree on Telecommunications

GFDM as a Framework for FBMC-OQAM: Iterative Detection and Performance Evaluation

Dissertation presented at the Instituto Nacional de Telecomunicações as part of the requirements for obtaining the Master's degree title.

Author: Ivo Bizon Franco de Almeida

Supervisor: Prof. Dr. Luciano Leonel Mendes

Co-supervisor: Prof. Dr. Guilherme Pedro Aquino

Santa Rita do Sapucaí

2018

Almeida, Ivo Bizon Franco de
A447g
GFDM as a Framework for FBMC-OQAM: Iterative Detection and Performance Evaluation. / Ivo Bizon Franco de Almeida. – Santa Rita do Sapucaí, 2018.
85 p.

Orientadores: Prof. Dr. Luciano Leonel Mendes e Prof. Dr. Guilherme Pedro Aquino.
Dissertação de Mestrado em Telecomunicações – Instituto Nacional de Telecomunicações – INATEL.
Inclui bibliografia.

1. Non-orthogonal waveforms 2. Multicarrier modulation 3. Message passing algorithms 4. Wireless communications 5. Mestrado em Telecomunicações. I. Mendes, Luciano Leonel e Aquino, Guilherme Pedro. II. Instituto Nacional de Telecomunicações – INATEL. III. Título.

CDU 621.39

Biblioteca "Ministro Olavo Bilac Pinto"

Ficha Catalográfica elaborada pelo Bibliotecário da Instituição
CRB6-2718 – Paulo Eduardo de Almeida

Approval Sheet

Dissertation presented and approved on December 19th, 2018.

Prof. Dr. Luciano Leonel Mendes
INATEL

Prof. Dr. Estevan Marcelo Lopes
INATEL

Prof. Dr. Gustavo Fraidenraich
State University of Campinas - UNICAMP

Prof. Dr. José Marcos Câmara Brito
Master's program coordinator

Santa Rita do Sapucaí
2018

To my parents and Jéssica.

Acknowledgements

The main acknowledgments are directed to my parents and Jéssica to whom I am very grateful for the support in my first step into the path of Science.

Special acknowledgments are directed to Prof. Luciano and Prof. Guilherme to whom I would like to thank for the enthusiastic encouragement, enlightening discussions and unwavering support during my research.

I would like to acknowledge Coordenação de Aperfeiçoamento de Pessoal de Nível Superior - Brasil (CAPES) - Finance Code 001, and the 5G-RANGE project (RNP and EC) for partially funding this work.

The creative way of life happens when the individual consistently, routinely, chooses the path of curiosity over the path of fear.

Elizabeth Gilbert

Abstract

This dissertation firstly presents a background on orthogonal frequency division multiplexing (OFDM), filter bank multicarrier with offset quadrature amplitude modulation (FBMC-OQAM) and generalized frequency division multiplexing (GFDM). Secondly, it exploits the flexibility of GFDM for generating a waveform that achieves the same performance as FBMC-OQAM, named Linear GFDM. Hence, enlarging the set of waveforms that can be derived from GFDM. Finally, based on the application of the sum-product algorithm (SPA) over factor graphs, the graphical representation of Linear GFDM followed by an iterative receiver algorithm, which does not require channel equalization nor noise variance as input information, are presented. Bit error ratio (BER), power spectral density (PSD) and peak-to-average ratio (PAPR) numerical estimation considering different channel models are used for validating the performance of Linear GFDM as well as the SPA-based detection algorithm.

Keywords: Non-orthogonal waveforms, Multicarrier modulation, Message passing algorithms, Wireless communications.

Resumo

Esta dissertação primeiramente apresenta um estudo nas técnicas *orthogonal frequency division multiplexing* (OFDM), *filter bank multicarrier with offset quadrature amplitude modulation* (FBMC-OQAM) e *generalized frequency division multiplexing* (GFDM). Em seguida esta dissertação, explora a flexibilidade do GFDM para gerar uma forma de onda que possui o mesmo desempenho do FBMC-OQAM, chamada de Linear GFDM. Aumentando, assim, o conjunto de formas de onda que podem ser derivadas do GFDM. Finalmente, baseado na aplicação do algoritmo soma-produto (SPA) sobre a representação em grafo-fator do Linear GFDM, propõe-se um algoritmo de recepção iterativo, que não necessita de equalização do canal nem da estimativa da variância do ruído como parâmetro entrada. Estimações numéricas da taxa de erro de bit (BER), densidade espectral de potência (PSD) e a relação entre a potência de pico e potencia média (PAPR) considerando diferentes modelos de canal são usados para validar o desempenho do Linear GFDM, bem como do algoritmo de detecção baseado no SPA.

Palavras-chave: Formas de onda não ortogonais, Modulação multiportadora, Algoritmos de passagem de mensagens, Comunicações sem fio.

List of Figures

Figure 1.1 – *Expected scenarios and services for 5G networks.* 2
Figure 2.1 – *Illustration of the OFDM transceiver diagram.* 9
Figure 2.2 – *Subcarrier spacing in FBMC-OQAM.* 11
Figure 2.3 – *Discrete time FBMC-OQAM transmitter diagram.* 11
Figure 2.4 – *Orthogonality among adjacent subcarriers in FBMC-OQAM.* 13
Figure 2.5 – *Discrete time FBMC-OQAM receiver diagram.* 13
Figure 2.6 – *Magnitude response from rectangular and Martin filter with different overlapping factors.* 15
Figure 2.7 – *Transmit matrix absolute value for $K = 4$ subcarriers, $M = 5$ subsymbols and Dirichlet pulse as prototype filter.* 17
Figure 2.8 – *GFDM transceiver block diagram.* 17
Figure 2.9 – *GFDM (a) and OFDM (b) frame illustration for low latency applications.* 20
Figure 3.1 – *GFDM-OQAM matrices absolute value for $M = 4$ subsymbols, $K = 6$ subcarriers and Martin pulse ($\Theta = 4$) as prototype filter.* 24
Figure 3.2 – *Linear GFDM transceiver block diagram.* 26
Figure 3.3 – *Linear matrices absolute value for $M = 4$ subsymbols, $K = 6$ subcarriers and Martin pulse ($\Theta = 4$) as prototype filter.* 26
Figure 3.4 – *Factor graph representation of Linear GFDM over AWGN channel.* . . . 29
Figure 3.5 – *Example of a factor graph.* 30
Figure 4.1 – *BER performance from Linear GFDM, FBMC-OQAM, GFDM and OFDM under AWGN channel.* 35
Figure 4.2 – *BER performance from Linear GFDM, FBMC-OQAM, GFDM and OFDM under time-invariant frequency-selective channel.* 36
Figure 4.3 – *BER performance from Linear GFDM, FBMC-OQAM, GFDM and OFDM under time-variant frequency-selective channel.* 36
Figure 4.4 – *Estimated PSD from Linear GFDM, FBMC-OQAM, GFDM and OFDM.* 37
Figure 4.5 – *Estimated PSD from Linear GFDM using different overlapping factors.* . 37
Figure 4.6 – *Estimated CCDF of the PAPR.* 38

Figure 4.7 – *BER performance from Linear GFDM under AWGN channel employing the SPA based demodulator.* 40
Figure 4.8 – *BER performance from Linear GFDM under Rayleigh channel employing the SPA based demodulator.* 41

List of Tables

Table 1.1 – *Gap between QoS indicators in 4G and 5G networks.* 4
Table 2.1 – *Frequency weighting coefficients.* 15
Table 2.2 – *Comparison among multicarrier waveforms.* 21
Table 4.1 – *Channel models I.* 34
Table 4.2 – *Waveform related simulation parameters I.* 34
Table 4.3 – *Channel models II.* 39
Table 4.4 – *Waveform related simulation parameters II.* 40

List of abbreviations and acronyms

1G	First Generation
2G	Second Generation
3G	Third Generation
4G	Fourth Generation
5G	Fifth Generation
AWGN	Additive Gaussian White Noise
BER	Bit Error Ratio
CCDF	Complementary Cumulative Distribution Function
CFO	Carrier Frequency Offset
CMT	Cosine Modulated Multitone
CP	Cyclic Prefix
CR	Cognitive Radio
CSI	Channel State Information
D2D	Device-to-Device
eMBB	enhanced Mobile Broadband
eRAC	extreme Remote Area Communications
FBMC	Filter Bank Multicarrier
FFT	Fast Fourier Transform

FI	Future Internet
FMT	Filtered Multitone
GFDM	Generalized Frequency Division Multiplexing
ICI	Intercarrier Interference
IoT	Internet of Things
ISI	Intersymbol Interference
LDPC	Low-Density Parity-Check
LTE	Long Term Evolution
MAP	Maximum A Posteriori
MF	Matched Filter
MIMO	Multiple Input Multiple Output
MMSE	Minimum Mean Square Error
mMTC	massive Machine Type Communications
mmWave	millimeter Wave
MPA	Message Passing Algorithm
NPR	Near Perfect Reconstruction
OFDM	Orthogonal Frequency Division Multiplexing
OOB	Out-Of-Band
OQAM	Offset Quadrature Amplitude Modulation
PAM	Pulse Amplitude Modulation
PAPR	Peak-to-Average Power Ratio
PHY	Physical Layer
PSD	Power Spectral Density
QoE	Quality of Experience
QoS	Quality of Service

RAT	Radio Access Technique
RC	Raised Cosine
RRC	Root-Raised-Cosine
SC-FDM	Single Carrier Frequency Division Multiplexing
SEP	Symbol Error Probability
SMT	Staggered Multitone
SMS	Short Message Service
SNR	Signal-to-Noise Ratio
SPA	Sum-Product Algorithm
TIFS	Time-Invariant Frequency-Selective
TVFS	Time-Variant Frequency-Selective
TVWS	Television White Spaces
URLLC	Ultra-Reliable Low-Latency Communications
VHF	Very High Frequency
VSB	Vestigial Side Band
XaaS	Anything as a Service
ZF	Zero Forcing

List of symbols

$x[n]$	Discrete time transmit signal
d_k	Complex-valued QAM symbol transmitted over the kth subcarrier
$g_k[n]$	Transmit filter impulse response modulated to the kth subcarrier
K	Number of subcarriers
$\mathrm{rect}[n]$	Discrete time rectangular function
$\exp(\cdot)$	Exponential function
j	Imaginary unit
N_{CP}	CP length in samples
N_{ch}	Channel impulse response length in samples
$y[n]$	Discrete time received signal
$h[n]$	Discrete time channel impulse response
$w[n]$	Discrete time AWGN signal
$\hat{d}_k$	Estimated QAM symbol from the kth subcarrier
$Y(k)$	Discrete Fourier transform of $y[n]$
$H(k)$	Channel frequency response
$W(k)$	Discrete Fourier transform of $w[n]$
R	Symbol rate
T	Symbol period

ΔF	Subcarrier spacing
$d_{k,m}$	QAM symbol transmitted over the kth subcarrier and mth time slot
$\Re\{\cdot\}$	Real part of $\{\cdot\}$
$\Im\{\cdot\}$	Imaginary part of $\{\cdot\}$
$g_{k,m}^{(\mathcal{I})}[n]$	In-phase transmit filter
$g_{k,m}^{(\mathcal{Q})}[n]$	Quadrature transmit filter
$p[n]$	Prototype filter impulse response
σ_w^2	AWGN variance
$\tilde{y}[n]$	Circular version of $y[n]$
$y_{\text{eq}}[n]$	Equalized received signal
$\hat{d}_{k,m}$	Estimated QAM symbol from the kth subcarrier and mth time slot
$(\cdot)^*$	Conjugate of $(\cdot)$
L_p	Prototype filter impulse response length in samples
Θ	Overlapping factor
$\bar{P}$	Frequency weighting coefficient
$\tilde{g}_{k,m}[n]$	Transmit filter circularly shifted to the mth time slot and modulated to the kth subcarrier
$\langle\cdot\rangle_N$	Modulo N circular shift
M	Number of subsymbols
$\mathbf{x}$	Transmit vector
$\mathbf{A}$	Transmit matrix
$\mathbf{d}$	Transmit data symbol vector
$\mathbf{g}_{k,m}$	Vector formed with samples from $\tilde{g}_{k,m}[n]$
$\mathbf{H}$	Circulant Toeplitz matrix from the channel impulse response

$\mathbf{y}$	Received vector
$\mathbf{w}$	AWGN vector
$\tilde{\mathbf{x}}$	Transmit vector after CP addition
$\tilde{\mathbf{w}}$	AWGN vector before CP removal
$\tilde{\mathbf{y}}$	Received vector before CP removal
$\mathbf{B}$	Demodulation matrix
$\mathcal{Y}$	Discrete Fourier transform of $\mathbf{y}$
$\mathcal{F}_N$	$N \times N$ Fourier matrix
$\mathcal{X}$	Discrete Fourier transform of $\mathbf{x}$
$\mathcal{W}$	Discrete Fourier transform of $\mathbf{w}$
$\mathcal{Y}_{\text{eq}}$	Equalized received vector in frequency domain
$(\cdot)^{\text{H}}$	Hermitian operator
$\mathbf{y}_{\text{eq}}$	Equalized received vector
$\hat{\mathbf{d}}$	Estimated data symbol vector
$\mathbf{B}_{\text{ZF}}$	Zero forcing demodulation matrix
$\mathbf{B}_{\text{MF}}$	Matched filter demodulation matrix
$\mathbf{B}_{\text{MMSE}}$	Minimum mean square error demodulation matrix
$\mathbf{R}_w$	Noise covariance matrix
J	QAM mapping index
E	Average energy of a J-QAM mapping
$\mathbf{I}_N$	$N \times N$ identity matrix
$\text{diag}\,(\cdot)$	Returns diagonal elements of a matrix
$d_{k,m}^{(\mathcal{I})}$	Real part of $d_{k,m}$
$d_{k,m}^{(\mathcal{Q})}$	Imaginary part of $d_{k,m}$
$\tilde{g}_{k,m}^{(\mathcal{I})}[n]$	Circular version of the in-phase transmit filter

$\tilde{g}_{k,m}^{(\mathcal{Q})}[n]$	Circular version of the quadrature transmit filter
$\mathbf{A}_{\mathrm{I}}$	In-phase transmit matrix
$\mathbf{A}_{\mathrm{Q}}$	Quadrature transmit matrix
$\mathbf{B}_{\mathrm{I}}$	In-phase demodulation matrix
$\mathbf{B}_{\mathrm{Q}}$	Quadrature demodulation matrix
L_Z	Zero valued sequence length
$\mathbf{A}_{\mathrm{I}}^{(\mathrm{L})}$	Linear in-phase transmit matrix
$\mathbf{A}_{\mathrm{Q}}^{(\mathrm{L})}$	Linear quadrature transmit matrix
$\mathbf{B}_{\mathrm{I}}^{(\mathrm{L})}$	Linear in-phase demodulation matrix
$\mathbf{B}_{\mathrm{Q}}^{(\mathrm{L})}$	Linear quadrature demodulation matrix
$\mathbf{x}_{\mathrm{I}}$	In-phase transmit vector
$\mathbf{x}_{\mathrm{Q}}$	Quadrature transmit vector
$\mathbf{\Psi}_{\mathrm{I}}$	In-phase equivalent matrix
$\mathbf{\Psi}_{\mathrm{Q}}$	Quadrature equivalent matrix
$\mathbf{y}_{\mathrm{I}}$	In-phase received vector
$\mathbf{y}_{\mathrm{Q}}$	Quadrature received vector
$\mathbf{H}^{(\mathrm{L})}$	Linear Toeplitz matrix from the channel impulse response
$\mathbf{d}^{(j)}$	jth variable node
f_i	ith factor node
$\mu_{f_i \to \mathbf{d}^{(j)}}^{(t)}\left(\mathbf{d}^{(j)}\right)$	Message from the factor node f_i to variable node $\mathbf{d}^{(j)}$ in the tth iteration
$\sum_{\sim\{x\}}$	*Summary* of x
$\|x\|$	Norm of x
$\mathbb{D}$	J-QAM mapping alphabet
$\mathbb{D}_{\mathrm{I}}$	Real part of $\mathbb{D}$

$\mathbb{D}_{\mathrm{Q}}$	Imaginary part of $\mathbb{D}$
$\mu^{(t)}_{\mathbf{d}^{(j)} \to f_i}\left(\mathbf{d}^{(j)}\right)$	Message from variable node $\mathbf{d}^{(j)}$ to factor node f_i in the tth iteration
τ	Number of iterations
$\mathbf{h}_{\mathrm{AWGN}}$	AWGN channel impulse response
$\mathbf{h}_{\mathrm{TIFS}}$	Time-invariant frequency-selective channel impulse response
$\mathbf{h}_{\mathrm{TVFS}}$	Time-variant frequency-selective channel impulse response
$\mathcal{CN}(0,1)$	Complex normal distribution with zero mean and unitary variance
α	Raised cosine filter roll off factor
β	Root raised cosine filter roll off factor
$\mathbf{h}_{\mathrm{Rayleigh}}$	Rayleigh channel impulse response
p_e	Symbol error probability
$\mathrm{erfc}(\cdot)$	Complementary error function
γ	Normalized signal-to-noise ratio
E_b	Average energy per bit
N_0	Thermal noise power spectral density
γ_r	Normalized signal-to-noise ratio for time-variant frequency-selective channel
ξ	Noise enhancement factor
ϕ_{ZF}	Zero forcing demodulation filter at the first subcarrier and subsymbol
ϱ	Normalized signal-to-noise ratio when noise enhancement is present
Φ_k	Frequency response of ϕ_{ZF} over the kth subcarrier
$\mathcal{C}$	Number of complex multiplications

Contents

1 INTRODUCTION 1
1.1 Motivation 1
1.2 Literature Revision 4
1.3 Scope and Objectives 5
1.4 Methodology 5
1.5 Summary of Contributions 6
1.6 Organization 6

2 BACKGROUND ON MULTICARRIER WAVEFORMS 7
2.1 Orthogonal Frequency Division Multiplexing 8
2.2 Filter Bank Multicarrier 10
2.3 Generalized Frequency Division Multiplexing 16
2.4 Chapter Summary 19

3 LINEAR GFDM AND SPA-BASED RECEIVER 23
3.1 Linear GFDM Definition 23
3.2 Sum-Product Algorithm Based Detector 27
3.3 Chapter Summary 32

4 PERFORMANCE EVALUATION 33
4.1 Linear GFDM Performance Evaluation 33
4.1.1 Bit Error Ratio 33
4.1.2 Spectral Containment 36
4.1.3 Peak-to-average Power Ratio 38
4.2 SPA Based Demodulator Performance Evaluation 39
4.2.1 Bit Error Ratio 39
4.2.2 Complexity 41
4.3 Chapter Summary 42

5 CONCLUSION AND FUTURE WORK 43

BIBLIOGRAPHY 45

A THEORETICAL SYMBOL ERROR PROBABILITY EXPRESSIONS 51
A.1 OFDM Symbol Error Probability 51
A.1.1 SEP over AWGN channel 51
A.1.2 SEP over frequency-selective channel 51
A.1.3 SEP over time-variant frequency-selective channel 52
A.2 GFDM Symbol Error Probability 52
A.2.1 SEP over AWGN Channel 52
A.2.2 SEP over frequency-selective channel 53
A.2.3 SEP over time-variant frequency-selective channel 53

Chapter 1

Introduction

1.1 Motivation

Since the early stages of mobile networks, its evolution has been driven by the necessity of larger data throughput. The first evolutionary step was given when digital transmission techniques were employed in the transition from the analogical first generation (1G) to the second generation (2G) of cellular networks. Digital voice services enhanced the user experience, and the launching of short message text (SMS) was a big success. About ten years after 2G, the third generation (3G) has had its start. The 3G mobile devices were then able to send multimedia content and browse the Internet. Also, mobile devices become more and more popular leading to a increase in the number of users. The fourth generation (4G) has increased the data rates significantly and, nowadays, smartphones can do a plethora of services using the mobile network. Since then, the possibilities of mobile communications were largely broaden and adoption by users was plentiful. As a consequence, the appetite for higher data throughput has increased.

The hunger for new or improved mobile services is driving the next generation of mobile networks. The fifth generation (5G) of cellular networks is expected to start its commercial deployment by 2020 [1]. 5G will not only be about an increase in data transmission. Rather, it will be a complete redefinition of the mobile network architecture that will provide support for emerging services and applications, as well as Future Internet (FI) access. For instance, the paradigm change from the client-server model to an anything as a service (XaaS) model represents one major step towards a networked society, where access to information is available to everyone, everywhere, at anytime [2][3]. It is important to emphasize that the network will encounter new usage patterns, since these novel services will

be either human driven or machine driven. Massive machine type communications (mMTC) will represent a considerable portion of data communications in the near future [4]. Specially in services/applications that demand controlling and monitoring. Therefore, it is necessary to engineer a network architecture that is flexible enough to sustain these new usage patterns [5].

Precisely, the services and applications that shall be supported by 5G networks can be divided in four different use-case scenarios. Namely, enhanced mobile broadband (eMBB), ultra-reliable low-latency communications (URLLC), extreme remote area communications (eRAC) and the afore mentioned mMTC [2][6][7]. Each scenario comes with its own operation requirements and particularities. Figure 1.1 illustrates the 5G scenarios and possible applications. Services that fall into the intercession of the Venn diagram are going to benefit from both scenarios.

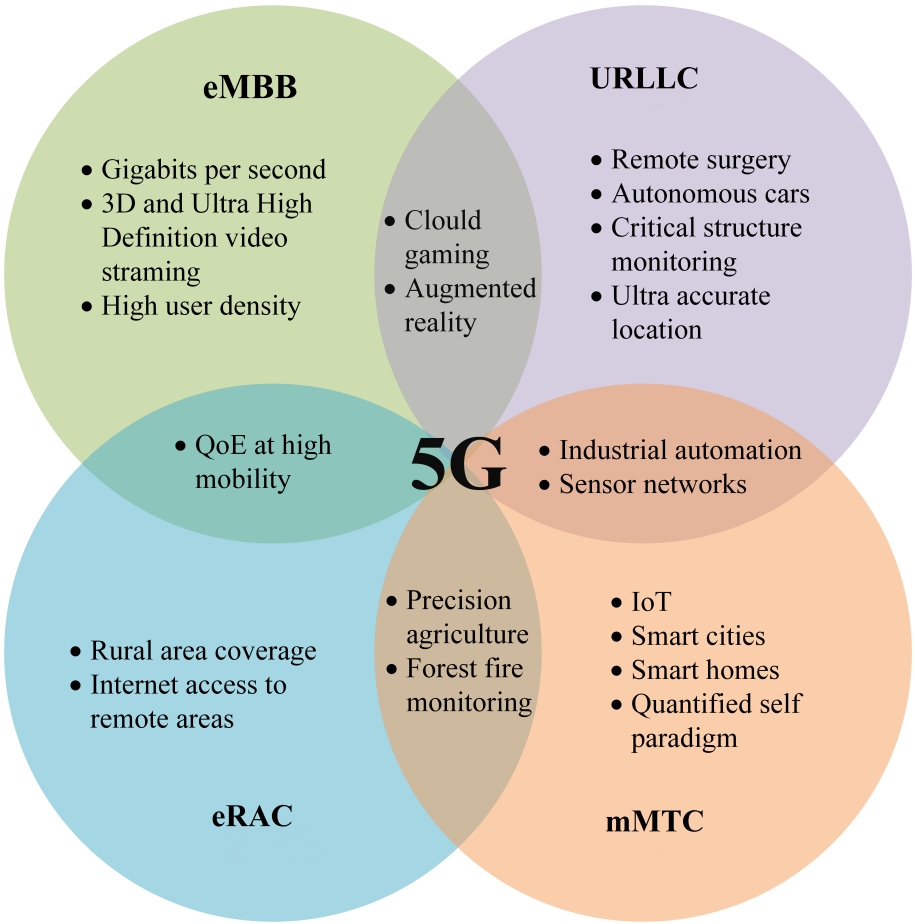

Figure 1.1 – *Expected scenarios and services for 5G networks.*

In general lines, the eMBB shall provide very large bandwidth allocation by operating with frequencies in the millimeter wave (mmWave) range [8], support for device-to-device (D2D) communication, massive multiple-input multiple-output

(MIMO), data rates up to 10 Gbps [9], latency in the order of 4 ms [10], seamless experience for users at mobility, quality of experience (QoE) even when moving at speeds up 500 km/h [6], spectrally and energetically efficient resource usage and support for content-aware applications [11]. Altogether, eMBB will attend general users for a much richer experience in all aspects when compared to previous generations.

URLLC will enable critical services over mobile networks. For instance, services such as remote surgery, self driven vehicles, delivery drones, wireless industry machinery monitoring and automation, augmented reality gaming and e-health applications shall be supported by this segment. These envisioned applications are critical and will be dealing with people's health in some cases. Hence, it will require overall latency less than 1 ms, ultra accurate device positioning and 99.999% reliability [7][12][13].

mMTC presents great challenge in 5G design due to its contrasting requirements. Despite, Internet of Things (IoT) represents the major design stimuli for this segment. IoT is a networking paradigm that is promising to change the way we experience technology in our daily lives. IoT can be defined as an integration of wired and wireless communication technologies, sensors and actuators that enable controlling and monitoring by mutual cooperation among *things* [14]. IoT devices will be pervasive, i.e., they will be in our houses, hospitals, streets, parking lots and factory plants. Consequently, the connectivity profile will change drastically from what is now experienced in 4G cellular networks, where most connected devices are smartphones that start new data transfers according to the owner's profile. Support device density in the order of 1 million devices per km^2, very high energy efficiency for allowing battery powered devices to remain active for at least 10 years without battery replacement are the primarily challenges [15][16].

eRAC represents the last frontier in telecommunications: be able to connect to the network even in the most remote locations. Internet access in remote areas will play an important role, for example, in precision agriculture, smart farming, forest fire prevention, environmental monitoring, wild life protection and precise location weather reports [17]. For achieving such connectivity in remote areas, opportunistic exploitation of television white spaces (TVWS) through cognitive radio (CR) is going to be critical. Thus, it is crucial to use a multicarrier technique that presents good spectral properties for reducing potential interference from opportunistic users into the primary users [18]. The very high frequency (VHF) bands can enable longer coverage for cellular networks. The expected coverage range for this scenario is about 50 km in radius, extending to 100 km with low

rate connectivity.

Table 1.1 shows the gap between quality of service (QoS) indicators experienced in 4G networks and the expected 5G QoS performance [19].

Table 1.1 – *Gap between QoS indicators in 4G and 5G networks.*

QoS indicator	4G	Gap	5G
Latency	30–50 ms	30–50×	1 ms
Mobility	350 km/h	1.5×	500 km/h
Number of connections	10^4 connections/km^2	100×	10^6 connections/km^2
Maximum data rate	100 Mbps	100×	10 Gbps
Coverage	10 km	5×	50 km

Given these points, a flexible approach for the physical layer (PHY) becomes an interesting solution, since a specific type of multicarrier modulation technique may not attend successfully to all requirements demanded by future applications.

1.2 Literature Revision

Recent literature on waveforms has been suggesting that fully orthogonal techniques, such as orthogonal frequency division multiplexing (OFDM), may not be the best option for the expected diversity of applications in 5G [20]. For this reason, advanced multicarrier modulation techniques that abandon full orthogonality have been extensively studied [21][22][23].

Filter bank multicarrier (FBMC) [24] is one of these non-orthogonal waveforms that has been considered for 5G in scenarios that require low out-of-band (OOB) emission, spectral efficiency, and robustness to carrier frequency offset (CFO). FBMC is often combined with offset quadrature amplitude modulation (OQAM) for achieving high spectral efficiency, if a long stream of data is assumed. Extensive investigation on FBMC techniques can be found in [25], [26] and [27].

Generalized frequency division multiplexing (GFDM) [28] is another non-orthogonal technique that has been proposed in the past decade [29], and it presents interesting characteristics that future wireless systems may benefit from. For instance, it has been introduced as a framework for other known waveforms, such as OFDM, single carrier frequency division multiplexing (SC-FDM), among other [30]. It fits best in scenarios were low latency, spectral efficiency and flexibility are the crucial characteristics.

Detection schemes based on message passing algorithms (MPA) have been notably employed for decoding of low-density parity-check (LDPC) codes [31]. In fact, MPAs represent a broader class with several algorithms, such as the expectation propagation, maximum-product and the sum-product algorithm (SPA), which is an generalization of the well known belief propagation algorithm. A very good tutorial content on SPA can be found in [32].

More recently these algorithms have been employed for detection of single carrier QAM modulated data symbols transmitted over doubly dispersive (time-variant and frequency-selective) channels [33], and also for demodulating other multicarrier waveforms, such as orthogonal time frequency space (OTFS) [34], GFDM [35] and OFDM [36].

1.3 Scope and Objectives

This work aims to enlarge the set of waveforms that can be generated through the GFDM framework by demonstrating how to generate FBMC-OQAM from GFDM's matrix formulation.

Additionally, it presents an iterative receiver algorithm based on the application of the SPA over factor graphs for demodulating complex-valued data symbols transmitted using either GFDM or FBMC-OQAM over doubly dispersive wireless channel.

For accomplishing such work, a complete understanding of these non-orthogonal multicarrier modulation techniques as well as the requirements and scenarios in which they will operate was achieved. Similarly, the graphical representation of these waveforms together with an algorithm tailored specific for them was obtained.

1.4 Methodology

Research on relevant literature on waveforms for 5G was employed as the main method for acquiring expertise on this topic. The same method was used for studying factor graphs and the SPA. Given the advanced formulation of such waveforms and decoding algorithm, numerical simulation using MATLAB® were employed for evaluating the performance of the FBMC-OQAM formulation through GFDM and of the estimation algorithm based on the SPA.

1.5 Summary of Contributions

The following papers were written as partial results from the research developed during the master's program.

- **Linear GFDM: A Low Out-of-band Emission Configuration for 5G Air Interface**. IEEE 1st 5G World Forum (WF-5G'18). Santa Clara, California, USA, July 9-11 2018.
- **5G Waveforms for IoT Applications**. IEEE Communications Surveys and Tutorials. Submitted on April, 2018. Minor revision and editing.
- **An Iterative Receiver for Non-Orthogonal Waveforms Based on the Sum-Product Algorithm**. In preparation for submission at the EURASIP Journal on Wireless Communications and Networking.

1.6 Organization

Chapter 2 presents a background on OFDM, and the characteristics that hinder its adoption as the only radio access technique (RAT) for 5G are discussed. In addition, a detailed study on FBMC and GFDM is conducted, and the employment of FBMC with OQAM is described.

Chapter 3 not only explores the flexible GFDM structure and proposes a modification for achieving identical performance as FBMC in aspects as ultra-low OOB emission and quasi-orthogonality, but also develops an iterative receiver algorithm using the SPA.

Chapter 4 presents discussions about the systems performance based on simulation results of the proposed schemes.

Chapter 5 concludes this dissertation and presents future work perspectives.

Chapter 2

Background on Multicarrier Waveforms

Certainly the future mobile structure will require a robust, yet flexible, RAT for addressing the envisioned services. Therefore, it is very likely that 5G networks will employ different multicarrier waveforms for each use-case scenario [20][37]. Multicarrier modulation techniques divide wide band signals, i.e., high data rate, into lower rate signals, where each occupies a narrower subband referred as subcarrier. This approach leads to robustness against frequency selective channels and flexibility for multiuser allocation. The current 4G PHY employs OFDM on the downlink, which has been extensively studied and widely deployed in wired and wireless communication systems. However, due to the wide range of requirements, some OFDM characteristics hinder its use in all the possible 5G divisions. The necessity of maintaining strict synchronism between users and the radio base station, elevated OOB emission and poor spectral efficiency when long cyclic prefix (CP) is required are the main OFDM shortcomings [38].

So far, OFDM will remain active in 5G systems [39]. This will partially enable eMBB use-case, giving to users a glimpse on what is yet to come in the future. Provided that scenarios have contradicting requirements, it is clear that flexibility is key for achieving the desired performance among all of them. Hence, this chapter presents a detailed background on OFDM, FBMC and GFDM, which are some candidate waveforms for the future 5G scenarios.

GFDM and FBMC-OQAM, differently from OFDM, are non-orthogonal waveforms, i.e., intrinsic intersymbol (ISI) and intercarrier (ICI) interference can arise. Nevertheless, by setting aside orthogonality, a new degree of freedom is achieved according to the Balian-Low theorem [40]. This means that FBMC and

GFDM can deliver good spectrum and time localization while presenting similar bit error ratio (BER) performance compared to orthogonal waveforms.

2.1 Orthogonal Frequency Division Multiplexing

OFDM [41] is the most employed multicarrier technique in either wireless and wired communication systems. Its acceptance comes from its simple transceiver design, which is usually built with the inverse and direct fast Fourier transform (FFT) algorithm that allows simple frequency domain equalization.

The OFDM discrete time transmit signal is given by

$$x[n] = \sum_{k=0}^{K-1} d_k g_k[n], \tag{2.1}$$

where d_k represents complex-valued data symbols, i.e., QAM symbols, that modulate the kth subcarrier, K is the total number of subcarriers. The transmit pulse at the kth subcarrier is given by

$$g_k[n] = \text{rect}[n] \exp\left(-j2\pi \frac{k}{K} n\right), \tag{2.2}$$

where rect$[n]$ is the discrete-time rectangular function, which is defined as

$$\text{rect}[n] = \begin{cases} 1, & \text{for } n = 0, \ldots, \ K-1 \\ 0, & \text{otherwise} \end{cases} \tag{2.3}$$

The high OOB emission of OFDM comes from the fact that it employs a rectangular window as transmission pulse, and therefore subcarriers are *sinc* shaped in frequency domain. Assuming transmission over time-dispersive channel, interference among OFDM symbols will occur. For dealing with this interblock interference, a copy of N_{CP} samples from the end of the OFDM symbol is placed at its beginning. Assuming that the channel impulse response has length N_{ch} samples, then $N_{\text{CP}} > N_{\text{ch}} - 1$ for ensuring interference free communication.

After CP removal, the convolution between the channel impulse response and the OFDM symbol becomes circular. For this reason, the observed channel at each subcarrier behaves like a single tap complex gain, and simple frequency domain equalization becomes possible. However, it is important to notice that the CP addition implies that spectral efficiency is reduced by the factor $K/(K + N_{\text{CP}})$.

At the receiver side, due to CP addition, the convolution between channel impulse response and transmit signal becomes circular yielding to

$$y[n] = h[n] \circledast x[n] + w[n], \tag{2.4}$$

where $h[n]$ represents the channel impulse response and $w[n]$ the additive white Gaussian noise (AWGN) samples. Let $Y(k) = \text{FFT}(y[n])$ represent the received signal in frequency domain. Hence, the estimated data symbol from the kth subcarrier is given by

$$\begin{aligned} \hat{d}_k &= \frac{Y(k)}{H(k)} \\ &= d_k + \frac{W(k)}{H(k)}, \end{aligned} \tag{2.5}$$

where $H(k)$ represents the channel frequency response and $W(k)$ is the discrete Fourier transform of $w[n]$.

The OFDM transceiver diagram is illustrated by Figure 2.1. Transmission and reception can be accomplished using the IFFT and FFT algorithms respectively.

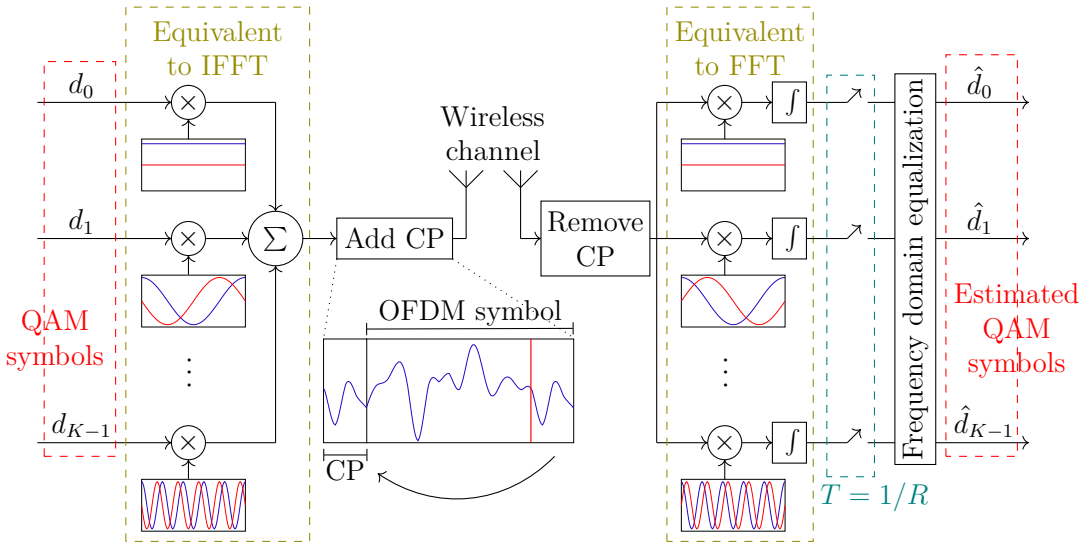

Figure 2.1 – *Illustration of the OFDM transceiver diagram.*

The synchronization process in 5G applications where energy consumption must reduced is expected to be more relaxed when compared to 4G long term evolution (LTE). Therefore, carrier frequency offset and multi user interference are likely to occur, and the RAT should be robust enough to cope with such impairments [22]. If proper synchronism between transmitter and receiver is satisfied, full orthogonality among subcarriers is then achieved. The synchronization process demands the reception of several OFDM frames and reference signals. The synchronization algorithm uses this information combined with the CP for estimating the beginning and the end of an OFDM symbol, as well to correct frequency misalignment. That process may take more time than the transmission

of useful information if the number of bits to be transmitted is small, e.g., in sensor networks applications [37]. This is undesirable if devices are power constrained as IoT applications where sensors collect data sporadicly and send it through the network [20][38]. Moreover, if unsynchronized transmissions occur, the interference to other subcarriers will lead to non negligible ICI due to high OOB emission of *sinc* shaped subcarriers. If one looks to opportunistic exploitation of vacant narrow spectrum holes, the OOB emission also represents a barrier [42]. Consequently, for some 5G scenarios, OFDM lacks the desired characteristics despite its straightforward design and well established employed. Nevertheless, the major OFDM advantages are the simple transceiver structure and straightforward combination with MIMO techniques [41].

2.2 Filter Bank Multicarrier

The primarily FBMC scheme was proposed by Chang [43] and further developed by Saltzberg [44] in around 1965, and it was rediscovered to be proposed as an alternative for future wireless communications by Bellanger [24].

Different variants of FBMC are described in literature, e.g., FBMC that operates in conjunction with regular QAM, called filtered multitone (FMT) [45][46], FBMC that uses pulse amplitude modulation (PAM), which is refereed as cosine modulated multitone (CMT) [47] and FBMC that operates in conjunction with OQAM, which is also called staggered multitone (SMT) [26].

FMT is build simply based on frequency division multiplexing. Each subcarrier is shaped using a filter with good frequency localization, i.e., a filter that is very contained in frequency domain. Half-Nyquist filters are used to form the transmitter and receiver filter banks and, therefore, ISI among subsequent QAM data symbols is avoided. However, FMT can only deliver half of the maximum spectral efficiency since neighboring subcarriers are not orthogonal, so non-negligible ICI arises. Considering a transmission rate of $R = 1/T$, the subcarrier spacing for ICI free transmission would be $\Delta F = 2/T$.

CMT was the first FBMC technique proposed in literature by Chang in 1966 [43]. His work describes the transmission of PAM modulated symbols using vestigial side band modulation (VSB). It can transmit real-valued symbols using minimally spaced subcarriers, i.e., $\Delta F = 1/2T$ for achieving maximum spectral efficiency.

SMT is the most studied variant for future wireless networks, and already

presents efficient implementations [26][27]. It was firstly proposed by Saltzberg [44], who has proposed the SMT scheme based on Chang's approach. SMT is commonly called in literature as FBMC-OQAM, OFDM-OQAM or simply FBMC. Henceforth, it will be referred as FBMC-OQAM.

FBMC-OQAM is able to transmit complex-valued symbols at a rate $R = 1/T$ with frequency spacing $\Delta F = 1/T$. Figure 2.2 presents a set of subcarriers distributed in frequency. The pulse shaping filter is chosen to be band limited for minimizing ICI among non adjacent subcarriers. However, neighboring subcarriers cause intrinsic ICI. If real-valued symbols are sent through odd multiples of ΔF and imaginary-valued symbols are sent through even multiples, then orthogonality among all subcarriers is restored. This separation of real and imaginary parts of complex-valued symbols leads to two-fold increase in the system's sampling rate.

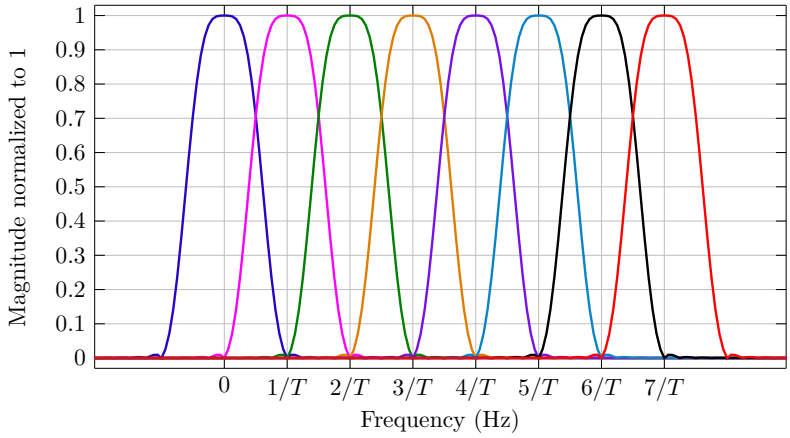

Figure 2.2 – *Subcarrier spacing in FBMC-OQAM.*

The transmission concept can be comprehended with the help of Figure 2.3, which illustrates the FBMC-OQAM discrete-time transmitter.

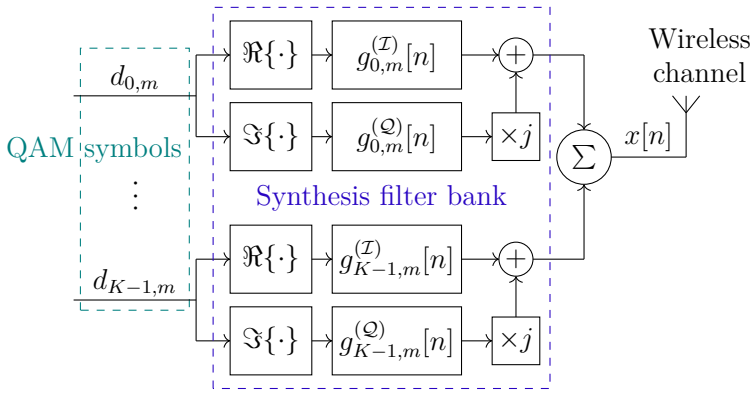

Figure 2.3 – *Discrete time FBMC-OQAM transmitter diagram.*

The discrete time transmit signal is given by

$$x[n] = \sum_{m=-\infty}^{+\infty} \sum_{k=0}^{K-1} \left\{ \Re\left\{d_{k,m}\right\} g_{k,m}^{(\mathcal{I})}[n] + j\Im\left\{d_{k,m}\right\} g_{k,m}^{(\mathcal{Q})}[n] \right\}, \tag{2.6}$$

where the input signals $d_{k,m}$ are complex-valued QAM symbols that are transmitted over the kth subcarrier and mth time slot, K represents the total number of subcarriers, and j is the imaginary unit. The transmit pulses for the in-phase and quadrature components are respectively given by

$$g_{k,m}^{(\mathcal{I})}[n] = p\left[n - mK\right] \exp\left(j2\pi \frac{k}{K} n + j\frac{\pi}{2}k\right) \tag{2.7}$$

$$g_{k,m}^{(\mathcal{Q})}[n] = p\left[n - \left(m + \frac{1}{2}\right)K\right] \exp\left(j2\pi \frac{k}{K} n + j\frac{\pi}{2}k\right), \tag{2.8}$$

where $p[n]$ represents the impulse response of the prototype filter.

In (2.7) and (2.8), the term $\exp\left(j2\pi\frac{k}{K}n\right)$ modulates the filter across the frequency spectrum, while the term $\exp\left(j\frac{\pi}{2}k\right)$ introduces a $\pi/2$ phase rotation between adjacent subcarriers. This phase rotation is called staggering, and it is responsible for ensuring orthogonality between adjacent subcarriers.

Mentioned earlier in this chapter, the Balian-Low theorem states that it is impossible to synthesize a limited function that presents simultaneously : *i*) good localization in time and frequency, *ii*) orthogonality in the complex field and *iii*) maximum spectral efficiency, i.e, $\Delta F = 1/T$ [40]. However, FBMC-OQAM circumvent the theorem using a relative delay between real and imaginary parts of the transmitted symbol. This relative delay is called offset, hence the name Offset QAM. Thus, orthogonality in the complex field is ensured and the filter design can be relaxed and focused on time and frequency localization.

For further clarify how FBMC-OQAM deals with the intrinsic ICI, Figure 2.4 illustrates the pulse given by the convolution between the transmit pulse over the kth and $(k+1)$th subcarrier for in-phase and quadrature components. As one can see in Figure 2.4 (a), the in-phase symbol transmitted over the kth does not cause ICI on the adjacent in-phase symbol at integer values of n/K. The same can be observed in Figure 2.4 (b) for the quadrature symbol component.

It is valid to point out that if time shifts and staggering are removed, and the prototype filter is replaced by a rectangular filter, the simplified FBMC-OQAM structure can be used to describe OFDM.

Figure 2.5 illustrates the discrete time receiver block diagram for FBMC-OQAM. Considering transmission over wireless channel, the discrete time received

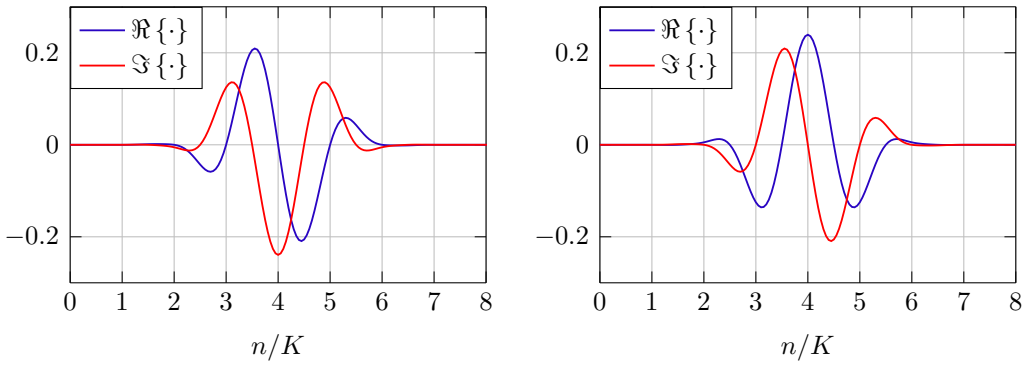

(a) $g^{(\mathcal{I})}_{k,m}[n] * g^{*(\mathcal{I})}_{k+1,m}[-n]$ (b) $jg^{(\mathcal{Q})}_{k,m}[n] * g^{*(\mathcal{Q})}_{k+1,m}[-n]$

Figure 2.4 – *Orthogonality among adjacent subcarriers in FBMC-OQAM.*

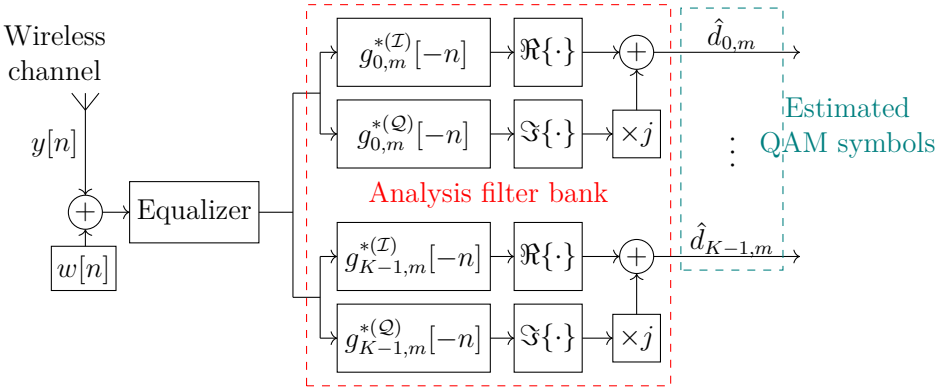

Figure 2.5 – *Discrete time FBMC-OQAM receiver diagram.*

signal is given by

$$y[n] = h[n] * x[n] + w[n], \tag{2.9}$$

where $h[n]$ represents the channel impulse response, $w[n]$ represents AWGN noise samples with zero mean and variance σ^2_w, and the operation $*$ denotes the linear convolution operation.

If the bandwidth per subcarrier is smaller than the channel coherence bandwidth, i.e., fading is considered flat per subcarrier, then simple zero forcing frequency domain equalization can be employed for equalizing the received signal. Otherwise, per subcarrier equalization must be used for canceling the channel induced distortion [25].

For generating circularity in the received signal, $N_{\text{ch}} - 1$ samples from the end of $y[n]$ are added to its beginning, where N_{ch} is the length of the channel impulse response, this procedure yields to $\tilde{y}[n]$. The equalized received signal is given by

$$y_{\text{eq}}[n] = \text{IFFT}\left(\frac{\text{FFT}\left(\tilde{y}[n]\right)}{\text{FFT}\left(h[n]\right)}\right) \tag{2.10}$$

The equalized received signal is filtered with matched filters modulated in each frequency slot, and rotated by $-\pi/2$ for annulling the staggering done at the transmitter. Hence, the estimated complex-valued QAM data symbols are given by

$$\hat{d}_{k,m} = \Re\left\{y_{\text{eq}}[n] * g_{k,m}^{*(\mathcal{I})}[-n]\right\} + j\Im\left\{y_{\text{eq}}[n] * g_{k,m}^{*(\mathcal{Q})}[-n]\right\}, \tag{2.11}$$

where $(\cdot)^*$ represents the complex conjugate operation.

For avoiding ISI, the pulse given by $p[n] * p^*[-n]$ must be real-valued and attend to the Nyquist criterion for ISI free transmission. The prototype filter plays an critical role on the spectral containment performance of FBMC schemes. For instance, one can employ the well known root-raised-cosine (RRC) filter as prototype. However, the filter proposed by Martin [48] is the most employed in FBMC-OQAM schemes due to its attenuated secondary lobes. The Martin filter is build based on the frequency sampling technique, and presents a very good suppression of side lobes. For this reason, it is largely employed in FBMC literature [25][49][50]. It is important to point out that this filter is classified as a non-perfect reconstruction (NPR) filter for maximally decimated systems. For multicarrier communications, this means that schemes which operate at the Nyquist rate suffer from intrinsic ISI caused by aliasing. However, the aliasing error generated by the filter is very small and it can be neglected when compared to impairments caused by the channel. The impulse response of the Martin filter has a closed form expression for cases where the filter order is 3, 4, 6 and 8 times greater than the number of subcarriers.

The filter is designed under the assumption of a frequency localization coefficient, which is called overlapping factor. The overlapping factor affects the length of the impulse response, meaning that the impulse response length will depend upon the overlapping factor. Assuming K subcarriers, the filter length is given by

$$L_p = \Theta K + 1, \tag{2.12}$$

where Θ represents the overlapping factor and K is the total number of subcarriers.

The filter impulse response is given by

$$p[n] = \bar{P}[0] + 2\sum_{i=1}^{\Theta-1}(-1)^i \bar{P}[i]\cos\left(\frac{2\pi i}{\Theta K}n\right), \tag{2.13}$$

where $\bar{P}[i]$ represents frequency weighting coefficients, and $n = 0, \ldots, \Theta K$ is the sample index.

Table 2.1 presents the frequency weighting coefficients for each overlapping factor [48]. Figure 2.6 illustrates the magnitude response considering different

Table 2.1 – *Frequency weighting coefficients.*

Coefficient	$\Theta = 3$	$\Theta = 4$	$\Theta = 6$	$\Theta = 8$
$\bar{P}[0]$	1	1	1	1
$\bar{P}[1]$	−0.91143783	−0.97195983	−0.99722723	−0.99988389
$\bar{P}[2]$	0.41143783	0.70710681	0.94136732	0.99315513
$\bar{P}[3]$		−0.23514695	−0.70710681	−0.92708081
$\bar{P}[4]$			0.3373834	0.70710681
$\bar{P}[5]$			−0.07441672	−0.37486154
$\bar{P}[6]$				0.11680723
$\bar{P}[7]$				−0.01523841

overlapping factors. For the sake of comparison, the magnitude response from a rectangular filter is also plotted. As one may note, as the overlapping factor increases, the stop-band attenuation of the filter also increases. An interesting characteristic is that the further in frequency one gets from the first lobe, the secondary lobes energy keeps decreasing. Hence, if it is employed as prototype filter, the resulting multicarrier waveform will present very low levels of OOB emission. As a result, high resolution exploitation of vacant spectrum holes may be possible in CR systems, for example.

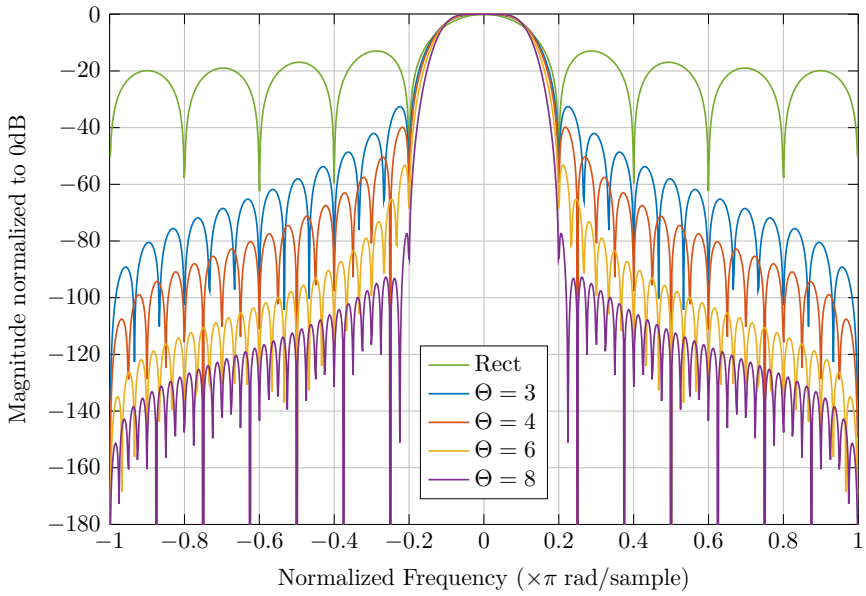

Figure 2.6 – *Magnitude response from rectangular and Martin filter with different overlapping factors.*

2.3 Generalized Frequency Division Multiplexing

GFDM is similar to FBMC in the sense that it is also based on filter bank theory, and, therefore, it is built upon a prototype filter. However, GFDM implements circular filtering, whereas FBMC implements linear filtering to shape each subcarrier. The GFDM modulation scheme distributes complex-valued data symbols in a time-frequency lattice, i.e., the waveform is composed by M versions of the prototype filter circularly shifted in M time-slots in K subcarriers. Each version is modulated by one data symbol. Thus, one GFDM multicarrier frame carries $N = KM$ complex-valued data symbols. Since the GFDM waveform is obtained through circular filtering, the transmit signal is also circular and contained in N samples. Hence, it is possible to insert a CP to protect the frame against multipath propagation impairments [51].

The discrete-time transmit signal before the CP addition is given by

$$x[n] = \sum_{k=0}^{K-1} \sum_{m=0}^{M-1} d_{k,m} \tilde{g}_{k,m}[n], \tag{2.14}$$

where $d_{k,m}$ represents complex-valued symbols that are sent through the kth subcarrier and mth subsymbol, $\tilde{g}_{k,m}[n]$ represents the prototype filter circularly shifted to the mth subsymbols and modulated to the kth subcarrier frequency and it is given by

$$\tilde{g}_{k,m}[n] = p\left[\langle n - mK \rangle_N\right] \exp\left(j2\pi \frac{k}{K} n\right), \tag{2.15}$$

where $p[n]$ is the prototype filter impulse response and $\langle \cdot \rangle_N$ represents the modulo N circular shift operation.

It is important to point out that depending on the prototype filter, its versions are not strictly orthogonal to each other in time or frequency domains. Therefore, intrinsic ISI and ICI may arise and cancellation techniques must be employed for dealing with these self interferences.

The transmission and reception mechanism can be described by matrix operations, which facilitates the analysis and the design of linear receiver designs, such as the minimum mean square (MMSE) demodulator. The transmit vector before the CP addition is given by

$$\mathbf{x} = \mathbf{A}\mathbf{d}, \tag{2.16}$$

where $\mathbf{d}$ represents the complex-valued data symbol vector with N elements, which come from QAM mapping. The N versions of the prototype filter can be arranged

in a $N \times N$ transmit matrix, leading to

$$\mathbf{A} = [\mathbf{g}_{0,0}\ \mathbf{g}_{1,0} \cdots \mathbf{g}_{K-1,0}\ \cdots\ \mathbf{g}_{0,M-1} \cdots \mathbf{g}_{K-1,M-1}], \tag{2.17}$$

where $\mathbf{g}_{k,m}$ represents the vector formed by samples from $\tilde{g}_{k,m}[n]$. The absolute value of the transmit matrix is shown in Figure 2.7 with Dirichlet pulse [51] as prototype filter.

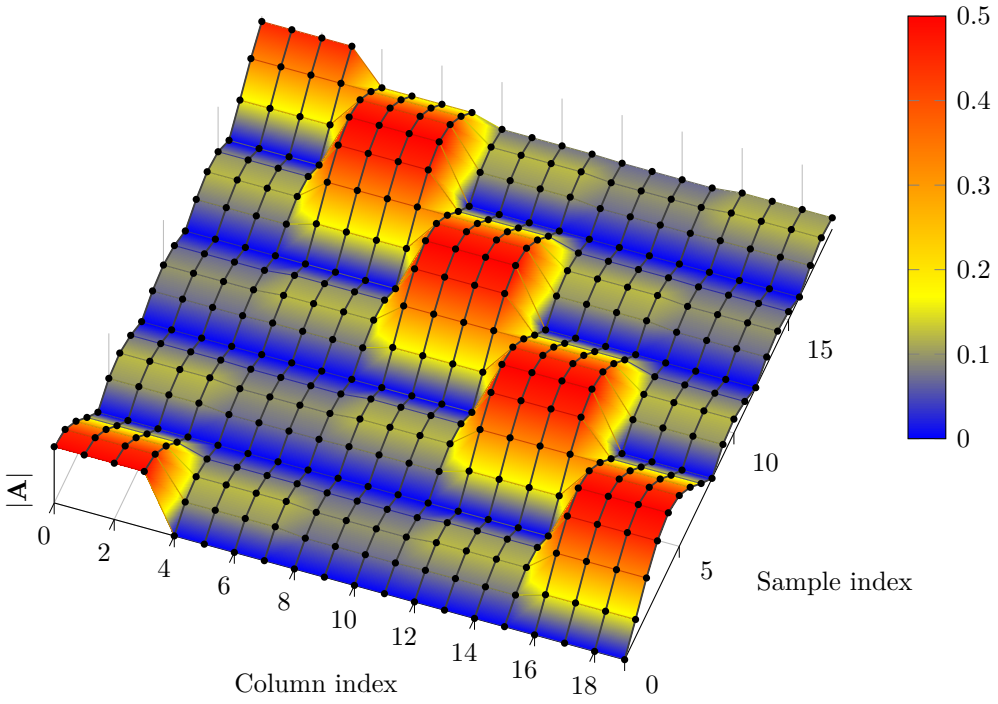

Figure 2.7 – *Transmit matrix absolute value for $K = 4$ subcarriers, $M = 5$ subsymbols and Dirichlet pulse as prototype filter.*

Figure 2.8 illustrates the GFDM transceiver block diagram [51].

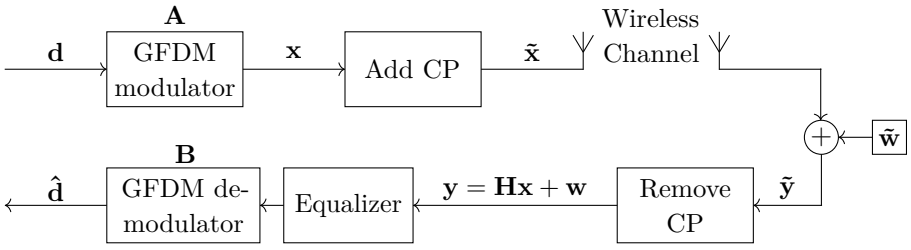

Figure 2.8 – *GFDM transceiver block diagram.*

The received signal after the CP removal is given by

$$\mathbf{y} = \mathbf{H}\mathbf{x} + \mathbf{w} \tag{2.18}$$

where, $\mathbf{H}$ is a circulant Toeplitz matrix from the channel impulse response and $\mathbf{w}$ represents the noise vector that follows a complex Gaussian distribution with

zero mean and variance σ_w^2. Note that after the CP removal, the channel matrix becomes circulant, and simple zero forcing frequency domain equalization can be used to eliminate channel induced distortion. Accordingly, the received vector in frequency domain is

$$\begin{aligned} \mathcal{Y} &= \mathcal{F}_N \mathbf{y} \\ &= \mathcal{F}_N \mathbf{H} \mathcal{F}_N^{\mathrm{H}} \mathcal{X} + \mathcal{W} \end{aligned} \tag{2.19}$$

where $\mathcal{F}_N$ and $\mathcal{F}_N^{\mathrm{H}}$ represent the $N \times N$ Fourier matrix and its conjugate transpose respectively, $\mathcal{X}$ and $\mathcal{W}$ represent $\mathbf{x}$ and $\mathbf{w}$ in frequency domain. Then, the equalized received vector in frequency domain is given by

$$\begin{aligned} \mathcal{Y}_{\mathrm{eq}} &= \left(\mathcal{F}_N \mathbf{H} \mathcal{F}_N^{\mathrm{H}}\right)^{-1} \mathcal{Y} \\ &= \mathcal{X} + \mathcal{F}_N \left(\mathbf{H}\right)^{-1} \mathcal{F}_N^{\mathrm{H}} \mathcal{W}, \end{aligned} \tag{2.20}$$

which yields to the equalized received vector in time domain

$$\begin{aligned} \mathbf{y}_{\mathrm{eq}} &= \mathcal{F}_N^{\mathrm{H}} \mathcal{Y}_{\mathrm{eq}} \\ &= \mathcal{F}_N^{\mathrm{H}} \mathcal{X} + \mathcal{F}_N^{\mathrm{H}} \mathcal{F}_N \left(\mathbf{H}\right)^{-1} \mathcal{F}_N^{\mathrm{H}} \mathcal{W} \\ &= \mathbf{x} + \left(\mathbf{H}\right)^{-1} \mathbf{w} \end{aligned} \tag{2.21}$$

The demodulation procedure is carried out by matrix operations as well. Defining $\mathbf{B}$ as the demodulation matrix, one can write

$$\begin{aligned} \hat{\mathbf{d}} &= \mathbf{B} \mathbf{y}_{\mathrm{eq}} \\ &= \mathbf{B} \left(\mathbf{x} + \left(\mathbf{H}\right)^{-1} \mathbf{w}\right) \\ &= \mathbf{B} \mathbf{A} \mathbf{d} + \mathbf{B} \left(\mathbf{H}\right)^{-1} \mathbf{w} \end{aligned} \tag{2.22}$$

Multiple demodulation matrices are described in literature [28][51]. The zero forcing (ZF) solution deals with the self generated ICI and ISI. On the other hand, it introduces noise enhancement due to its non-contained frequency responses.

The matched filter (MF) solution maximizes the signal to noise ratio and does not collect noise from other subcarriers. Still, it does not handle the ICI and ISI generated by non-orthogonal prototype filters. It worth mention that if the prototype filter respects the Nyquist criterion for ISI free transmission, ISI is avoided but ICI remains.

Although a more complex approach, the MMSE demodulation matrix is able to cancel self interference while keeping noise enhancement at low level.

Respectively, the demodulation matrices for ZF, MF and MMSE receivers are given by

$$\mathbf{B}_{\mathrm{ZF}} = \mathbf{A}^{-1} \tag{2.23}$$

$$\mathbf{B}_{\mathrm{MF}} = \mathbf{A}^{\mathrm{H}} \tag{2.24}$$

$$\mathbf{B}_{\mathrm{MMSE}} = \left(\mathbf{R}_w + \mathbf{A}^{\mathrm{H}}\mathbf{H}^{\mathrm{H}}\mathbf{H}\mathbf{A}\right)^{-1}\mathbf{A}^{\mathrm{H}}\mathbf{H}^{\mathrm{H}}, \tag{2.25}$$

where $(\cdot)^{\mathrm{H}}$ is the Hermitian conjugate transpose operation and the covariance matrix of the noise is given by

$$\mathbf{R}_w = \frac{\sigma_w^2}{EN}\mathbf{I}_N, \tag{2.26}$$

where E is the average energy of the J-QAM mapping, $N = KM$, and $\mathbf{I}_N$ represents a $N \times N$ identity matrix.

It is important to point out that the MMSE demodulator is a biased estimator, so compensation in the demodulated data symbols becomes necessary. In addition, MMSE demodulation takes in consideration the channel matrix ($\mathbf{H}$). Thus, previous equalization is not necessary and the estimated data symbols can be retrieved directly from the received vector, yielding to

$$\hat{\mathbf{d}} = \frac{\mathbf{B}_{\mathrm{MMSE}}\mathbf{y}}{\mathrm{diag}\left(\mathbf{B}_{\mathrm{MMSE}}\mathbf{A}\mathbf{H}\right)}, \tag{2.27}$$

where $\mathrm{diag}\left(\cdot\right)$ forms a vector with the samples from the diagonal of a matrix. Although it presents better performance than MF and ZF, the implementation complexity of the MMSE receiver is greater. The MMSE demodulator requires a matrix inversion when the channel impulse response changes, and it needs the estimation of the noise variance.

The number of subsymbols and subcarriers is an important design concern for GFDM. It is demonstrated in [52] that when K and M are even the modulation matrix becomes singular, and hence non-invertible. Therefore, the ZF demodulator does not exist, and the MF performs poorly. However, this issue was addressed in [53]. Furthermore, for a fixed number of subcarriers, the smaller M values will lead to better performance when the ZF is employed [51].

2.4 Chapter Summary

OFDM can be classified as subcase of either FBMC or GFDM. For instance, if the diagram shown in Figure 2.3 is simplified and the prototype filter is set

to a rectangular filter, then the resulting waveform will be OFDM. Similarly for GFDM, if the number of subsymbols is set to one ($M = 1$, $K = N$) and prototype filter is set to a rectangular filter, the same result is obtained. Moreover, making $K = 1$, $M = N$ and the Dirichelet pulse as prototype filter, GFDM leads to single carrier frequency division multiplexing (SC-FDM) [54].

By setting aside orthogonality, a new degree of freedom is achieved according to the Balian-Low theorem [40], and waveforms that present good time and frequency localization and operate at the Nyquist rate can be synthesized. Thus, OOB emission, efficient resource utilization, relaxed synchronism, robustness against intrinsic interference can be achieved [20]. Therefore, GFDM and FBMC are clearly more complete than OFDM. GFDM and FBMC present characteristics in terms of OOB emission, spectral efficiency, flexibility and latency that are attractive for next generations of cellular networks, despite their elaborated schemes.

Note that the CP is present in the GFDM frame, which degrades the spectral efficiency in exchange of robustness against ISI. However, the CP that would protect K data symbols in OFDM will protect MK data symbols in GFDM. Therefore, spectral efficiency can be improved.

For instance, applications from URLLC scenario may benefit from GFDM's scheme when short packets are transmitted since latency is direct related to frame size, as illustrated by Figure 2.9.

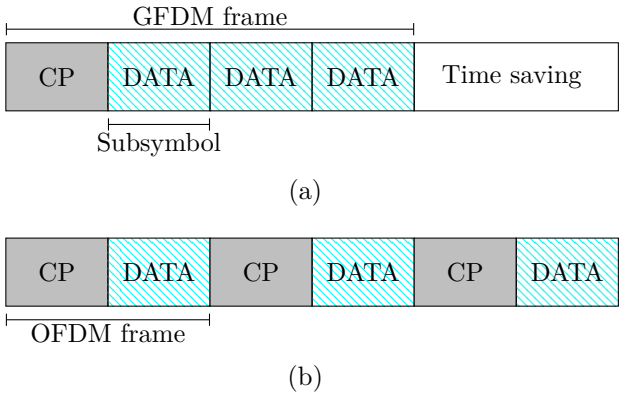

Figure 2.9 – *GFDM (a) and OFDM (b) frame illustration for low latency applications.*

Considering FBMC-OQAM, the spectral efficiency can approach the unity if a long stream of data is transmitted. FBMC-OQAM only falls short in terms of spectral efficiency when short packets of data are transmitted sporadically. This performance loss is due to the ramp-up and ramp-down time of the filters used to

shape the subcarriers. As mentioned, prototype filter with good frequency localization is employed in FBMC-OQAM, therefore the resulting transmit waveform will present very low levels of OOB emission. As a result, high resolution exploitation of vacant spectrum holes may be possible in CR systems with FBMC-OQAM. In addition, rough synchronized transmission can be accomplished without causing prohibitive interference to other users [55].

In the next chapter GFDM will be modified for achieving the same performance of FBMC-OQAM. Thus, showing its flexibility and capability to adapt to the requirements of different application scenarios.

Table 2.2 presents a summarized comparison of the main characteristics regarding the afore presented waveforms.

Table 2.2 – *Comparison among multicarrier waveforms.*

Characteristic	OFDM	GFDM	FBMC-OQAM
Orthogonality	Orthogonal	Non-orthogonal	Quasi-orthogonal
Mapping scheme	QAM	QAM	OQAM
Cyclic prefix	Yes	Yes	No
Transmission Efficiency	$\frac{K}{K+N_{\mathrm{CP}}}$	$\frac{MK}{MK+N_{\mathrm{CP}}}$	$\frac{\text{Data packet}}{\text{Data packet} + L_p}$
Prototype filter	Rectangular	Arbitrary	Half Nyquist
Prototype filter convolution	Cyclic	Cyclic	Linear
OOB emission	Worst due to cyclic rectangular filtering	Better than OFDM but limited due to cyclic filtering	Best due to linear subcarrier wise filtering
Waveform length	$K + N_{\mathrm{CP}}$	$MK + N_{\mathrm{CP}}$	Data packet + L_p – 1

Chapter 3

Linear GFDM and SPA-based Receiver

GFDM and FBMC present attractive characteristics for enabling future wireless applications. Consequently, this chapter contributes with the current literature by presenting GFDM as a framework for generating FBMC-OQAM, as well as presenting an iterative receiver algorithm based on the SPA.

3.1 Linear GFDM Definition

The GFDM structure can be used to obtain a transmit signal that presents the same characteristics of FBMC-OQAM, specially in terms of spectral containment. Time-domain OQAM for GFDM [51][56] needs to be introduced before the GFDM structure be further modified to achieve the same performance as FBMC-OQAM.

Similarly to OQAM description of Section 2.2, the complex-valued data symbols need to be separated into its real and imaginary parts, since each part will modulate a different transmit filter. This separation yields to $d_{k,m}^{(\mathcal{I})} = \Re\{d_{k,m}\}$ and $d_{k,m}^{(\mathcal{Q})} = \Im\{d_{k,m}\}$, where $d_{k,m}$ represents complex-valued symbols from QAM mapping that are transmitted over the kth subcarrier and mth subsymbol.

The transmit filters for the in-phase and quadrature components are described based on the prototype filter response, leading to

$$\tilde{g}_{k,m}^{(\mathcal{I})}[n] = p\left[\langle n - mK\rangle_N\right] \exp\left(j2\pi\frac{k}{K}n + j\frac{\pi}{2}k\right) \tag{3.1}$$

$$\tilde{g}_{k,m}^{(\mathcal{Q})}[n] = p\left[\left\langle n - \left(m + \frac{1}{2}\right)K\right\rangle_N\right] \exp\left(j2\pi\frac{k}{K}n + j\frac{\pi}{2}k\right). \tag{3.2}$$

Finally, the discrete time GFDM-OQAM transmit signal is given by

$$x[n] = \sum_{m=0}^{M-1} \sum_{k=0}^{K-1} d_{k,m}^{(\mathcal{I})} \tilde{g}_{k,m}^{(\mathcal{I})}[n] + j \sum_{m=0}^{M-1} \sum_{k=0}^{K-1} d_{k,m}^{(\mathcal{Q})} \tilde{g}_{k,m}^{(\mathcal{Q})}[n]. \tag{3.3}$$

Each part of the transmit data symbol independently modulates transmit filters, which are circularly shifted in time by half subsymbol in relation to each other. Also a $\pi/2$ phase shift is introduced among adjacent subcarriers. This arrangement avoids neighboring ICI by transmitting real-valued and imaginary-valued data over adjacent subcarriers, and the non-neighboring ICI that would arise from non-orthogonal subcarriers is avoided if the prototype filter has good frequency localization. Furthermore, if half-Nyquist pulse is used as prototype filter, then ISI among successive data symbols is also avoided with matched filter receiver in flat fading channels.

The matrix notation for obtaining time-domain OQAM implementation for GFDM is achieved by employing two different modulation matrices, denoted by $\mathbf{A}_{\mathrm{I}}$ and $\mathbf{A}_{\mathrm{Q}}$, where the quadrature matrix $\mathbf{A}_{\mathrm{Q}}$ is half subsymbol (or $K/2$ samples) circularly shifted in relation to the in-phase matrix $\mathbf{A}_{\mathrm{I}}$. These matrices are obtained from the filters $\tilde{g}_{k,m}^{(\mathcal{I})}[n]$ and $\tilde{g}_{k,m}^{(\mathcal{Q})}[n]$ similarly to (2.17). The matrices absolute value are shown in Figure 3.1.

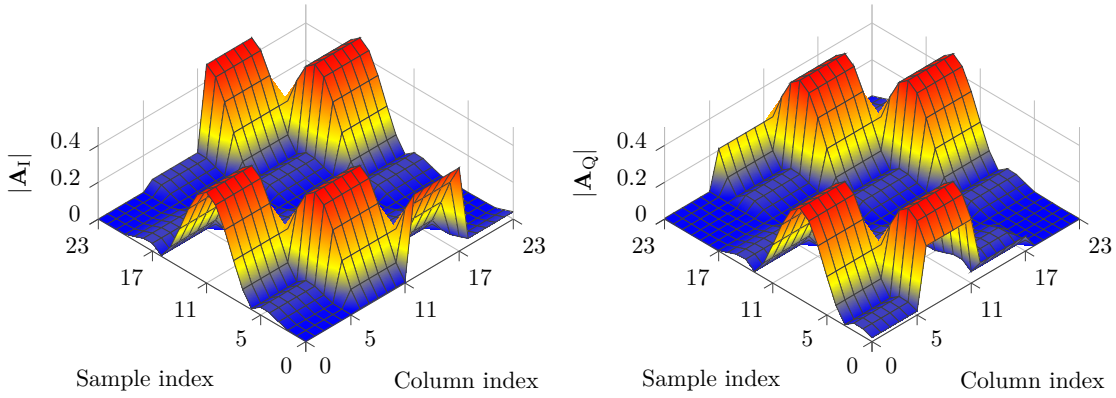

(a) *Absolute value of* $\mathbf{A}_{\mathrm{I}}$. (b) *Absolute value of* $\mathbf{A}_{\mathrm{Q}}$.

Figure 3.1 – *GFDM-OQAM matrices absolute value for* $M = 4$ *subsymbols,* $K = 6$ *subcarriers and Martin pulse* ($\Theta = 4$) *as prototype filter.*

$\mathbf{A}_{\mathrm{I}}$ is modulated by the real part of a complex-valued QAM symbol, while $\mathbf{A}_{\mathrm{Q}}$ is modulated by the imaginary part. The transmit vector is then obtained as

$$\mathbf{x} = \mathbf{A}_{\mathrm{I}} \Re\{\mathbf{d}\} + j\mathbf{A}_{\mathrm{Q}} \Im\{\mathbf{d}\} \tag{3.4}$$

At the receiver side, frequency domain equalization can be employed if a CP is used for protecting the transmit signal from the channel induced time

dispersion. The equalized received vector is demodulated by a matched filter matrix, leading to

$$\hat{\mathbf{d}} = \Re\left\{\mathbf{B}_{\mathrm{I}}\mathbf{y}_{\mathrm{eq}}\right\} + j\Im\left\{\mathbf{B}_{\mathrm{Q}}\mathbf{y}_{\mathrm{eq}}\right\}, \tag{3.5}$$

where $\mathbf{B}_{\mathrm{I}} = \mathbf{A}_{\mathrm{I}}^{\mathrm{H}}$ and $\mathbf{B}_{\mathrm{Q}} = \mathbf{A}_{\mathrm{Q}}^{\mathrm{H}}$.

As one may notice in Figure 3.1, transmit matrices have abrupt transitions at the edges, which leads to discontinuities in the transmitted signal. For this reason, the GFDM-OQAM transmit signal presents undesirable levels of OOB emission.

Zero padding the prototype filter without modifying its frequency localization is possible. Hence, let L_Z denote the length of the zero-valued sequence that is padded to $p[n]$. To ensure no circularity, i.e., no abrupt transitions in a given GFDM modulation matrix, L_Z is given by

$$L_Z = K(M-1). \tag{3.6}$$

However, the matrix $\mathbf{A}_{\mathrm{Q}}$ is shifted by half subsymbol in relation to $\mathbf{A}_{\mathrm{I}}$, and it is necessary to add extra $K/2$ zeros, yielding to

$$L_Z = K(M-1) + K/2 = KM - K/2 \tag{3.7}$$

Therefore, both matrices show smooth transitions at edges and a linear filtering behavior is obtained.

Let $\mathbf{A}_{\mathrm{I}}^{(\mathrm{L})}$ and $\mathbf{A}_{\mathrm{Q}}^{(\mathrm{L})}$ represent the modified modulation matrices obtained from the zero padded transmit pulses. Figure 3.3 illustrates their absolute value. As one can observe, the modified transmit matrices present linear time-shift among subsymbols. Hence, smooth transitions are observed in the transmit vector, and OOB emission is drastically reduced.

The block diagram for the Linear GFDM modulation scheme is depicted in Figure 3.2. The transmit and received vectors are obtained similarly to (3.4) and (3.5). Demodulation matrices for the Linear GFDM configuration are also matched filter matrices obtained similarly to (2.23).

One of the main differences between the GFDM-OQAM and Linear GFDM is that the former is circular and frequency domain equalization can be used when a CP protects the transmitted signal. On the other hand, Linear GFDM needs to emulate circular convolution with the channel impulse response in order to apply frequency domain equalization. This procedure is the same described for FBMC-OQAM in Section 2.2. When the Martin pulse is used as prototype filter, the overlapping factor translates to the number of subsymbols. Therefore, for

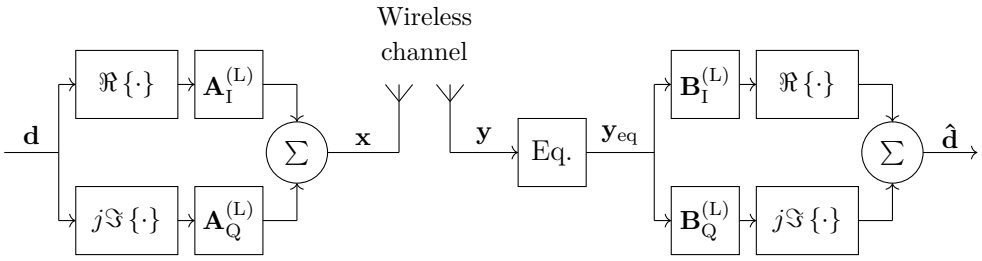

Figure 3.2 – *Linear GFDM transceiver block diagram.*

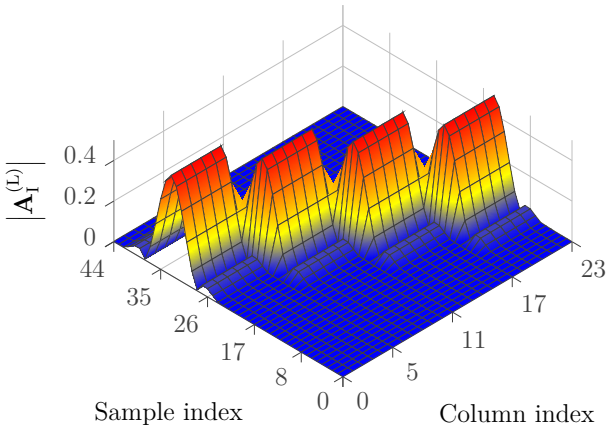

(a) Absolute value of $\mathbf{A}_{\mathrm{I}}^{(\mathrm{L})}$.

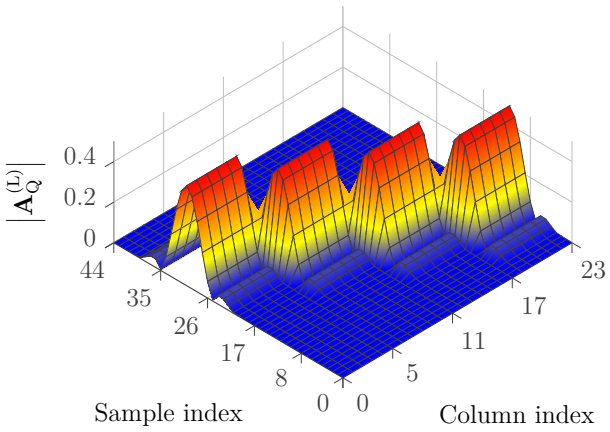

(b) Absolute value of $\mathbf{A}_{\mathrm{Q}}^{(\mathrm{L})}$.

Figure 3.3 – *Linear matrices absolute value for* $M = 4$ *subsymbols,* $K = 6$ *subcarriers and Martin pulse* $(\Theta = 4)$ *as prototype filter.*

Linear GFDM, the higher values of M will lead to lower levels of OOB emission. Furthermore, since the transmit data symbols are split into its real and imaginary parts, the number of subcarriers must be even. Comparing Linear GFDM with the conventional GFDM scheme described in Section 2.3, given the extension of the prototype filter, the resulting Linear GFDM transmit vector will be longer than the GFDM symbol. This characteristic may increase the overall latency of

communication systems employing Linear GFDM.

3.2 Sum-Product Algorithm Based Detector

Linear demodulation solutions for the mentioned waveforms are well-known. However, most of these approaches need channel equalization prior to demodulation, and equalizers often need the noise variance estimation, e.g., the MMSE equalizer [57].

This section presents an iterative detection algorithm based on the sum-product algorithm (SPA) that operates over factor graphs for estimating complex-valued data symbols, i.e., QAM symbols, modulated using the matrix formulation of GFDM. The proposed algorithm can be employed for either GFDM or FBMC-OQAM demodulation, since Linear GFDM is the GFDM variant equivalent to FBMC-OQAM. This Section tailors an algorithm for Linear GFDM, since it presents benefits in terms of complexity due to the separation of real and imaginary parts of the transmitted QAM symbols.

The SPA is an instance of message passing algorithms, which are often employed in the machine learning literature for estimating marginal probabilities on factor graphs [32][58][59]. Factor graphs can be defined as a graphical representation of the relation among a set of variables in a probabilistic model. It is a bipartite graph composed by variable nodes and function factor nodes, function nodes are often referred as factor nodes. If, and only if, a variable appears in a factor, an undirected edge connects them. In factor graph representation, variable nodes are represented by circles and factor nodes are represented by filled squares.

The SPA operates by propagating messages along this edges. The outcome of this algorithm will be the marginal probability distribution related to each variable node in the graph. If the factor graph is cycle free, the algorithm converges to the exact marginal distribution related to each variable. Whereas if the graph naturally contains cycles, an iterative schedule shall be used for estimating the marginals.

Many well known algorithms in coding and estimation theory may be viewed as specific instances of message passing on factor graphs. Furthermore, factor graph representation of wireless systems leads to a combined representation of channel influence, modulation and coding [60].

The estimation problem in non-orthogonal multicarrier modulation schemes can be formulated as a problem of inference in graphical models. Based on a set of

received signal samples, the receiver algorithm wishes to infer the transmitted data symbols using the SPA operating on its factor graph representation. Therefore, the description of Linear GFDM as a factor graph is mandatory.

The Linear GFDM transmit vector is obtained by adding its in-phase with the quadrature component, similarly to (3.4), which yields to

$$\mathbf{x} = \mathbf{A}_{\mathrm{I}}^{(\mathrm{L})} \Re\{\mathbf{d}\} + j\mathbf{A}_{\mathrm{Q}}^{(\mathrm{L})} \Im\{\mathbf{d}\} = \mathbf{x}_{\mathrm{I}} + \mathbf{x}_{\mathrm{Q}}. \tag{3.8}$$

Following Figure 3.2, at receiver side, the received vector prior to equalization can be written as

$$\mathbf{y} = \mathbf{\Psi}_{\mathrm{I}} \Re\{\mathbf{d}\} + j\mathbf{\Psi}_{\mathrm{Q}} \Im\{\mathbf{d}\} + \mathbf{w} = \mathbf{y}_{\mathrm{I}} + \mathbf{y}_{\mathrm{Q}} + \mathbf{w}, \tag{3.9}$$

where $\mathbf{w}$ represents the AWGN noise vector and the *equivalent* matrices are defined as

$$\mathbf{\Psi}_{\mathrm{I}} = \mathbf{H}^{(\mathrm{L})} \mathbf{A}_{\mathrm{I}}^{(\mathrm{L})} \tag{3.10}$$

$$\mathbf{\Psi}_{\mathrm{Q}} = \mathbf{H}^{(\mathrm{L})} \mathbf{A}_{\mathrm{Q}}^{(\mathrm{L})} \tag{3.11}$$

with $\mathbf{H}^{(\mathrm{L})}$ representing the linear Toeplitz matrix from the channel impulse response. For the sake of brevity, the notation $(\cdot)^{(\mathrm{L})}$ was omitted in $\mathbf{\Psi}_{\mathrm{I}}$ and $\mathbf{\Psi}_{\mathrm{Q}}$.

For representing Linear GFDM with a factor graph, there is one particular graph for each equivalent matrix. The non-zero values of each matrix will determine the edges that connect factor nodes to variable nodes. Consequently, real and imaginary parts are estimated separately. The SPA will estimate marginal probabilities related to each variable node of the graph. Hence, it is possible to use the maximum a posteriori criterion (MAP) for estimating the most likely transmitted data symbol. The factor graph that represents the relation among the real part of the data symbol vector and in-phase component of the received vector is illustrated in Figure 3.4 (a) considering $K = 2$ subcarriers, $M = 3$ subsymbols and Martin pulse as prototype filter. Note that the first two samples of the received vector do not receive any contributions due to the linear filtering behavior. The graph for the imaginary part and quadrature component is constructed similarly, and it is shown in Figure 3.4 (b). It important to point out that the transmit vector has length given by $L_{\mathbf{x}} = KM + KM - K/2$. Hence, for the given example, the graph contains eleven factor nodes from the received signal samples and six variable nodes from the data vector.

The SPA will estimate the marginal distribution for each variable node in the graph by passing messages from factor nodes to variable nodes. The message

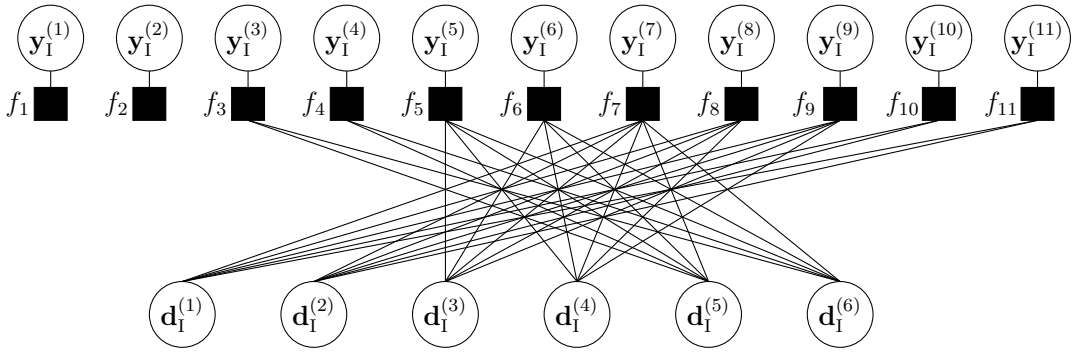

(a) *Relation among* $\mathbf{y}_{\mathrm{I}}$ *and* $\mathbf{d}_{\mathrm{I}} = \Re\{\mathbf{d}\}$.

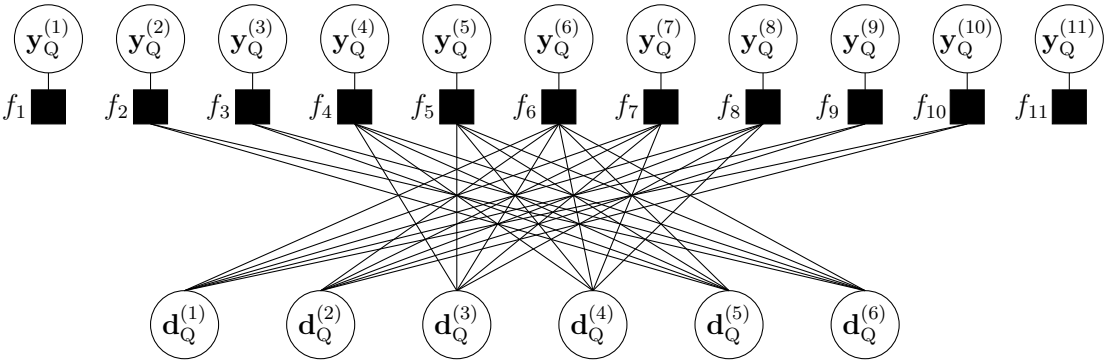

(b) *Relation among* $\mathbf{y}_{\mathrm{Q}}$ *and* $\mathbf{d}_{\mathrm{Q}} = \Im\{\mathbf{d}\}$.

Figure 3.4 – *Factor graph representation of Linear GFDM over AWGN channel.*

passing schedule starts with variable nodes sending initial unit messages to factor nodes, which in turn calculate the beliefs of each one and pass back along the edges.

Granted that channel state information is available at the receiver, messages from the factor node f_i to variable node $\mathbf{d}^{(j)}$ over the tth iteration are calculated as follows

$$\mu^{(t)}_{f_i \to \mathbf{d}^{(j)}}\left(\mathbf{d}^{(j)}\right) = \sum_{\sim\left\{\mathbf{d}^{(j)}\right\}} \left\{ \exp\left(-\left\| \mathbf{y}^{(i)} - \sum_{k \in N(f_i)} \mathbf{\Psi}^{(i,k)} \mathbf{d}^{(k)} \right\|^2 \right) \right\} \times \prod_{u \in N(f_i)\backslash j} \mu^{(t-1)}_{\mathbf{d}^{(u)} \to f_i}\left(\mathbf{d}^{(u)}\right), \quad (3.12)$$

where ith sample from the received vector is represented by $\mathbf{y}^{(i)}$, the ith factor node is represented by f_i, and $\mathbf{\Psi}^{(i,k)}$ represents the element in the ith line and kth column of $\mathbf{\Psi}$. The notation $N(f_i)\backslash j$ represents the set of variable nodes connected to f_i excluding the jth node. Messages must be calculated for the in-phase and quadrature components. However, in (3.12) the subindices (I) and (Q) were removed for the sake of brevity. The sum in (3.12) is carried over an alphabet of possible values assumed by $\mathbf{d}^{(k)}$. The alphabets for the in-phase and

quadrature components are described as

$$\mathbb{D}_{\mathrm{I}} \in \Re\{\mathbb{D}\} \tag{3.13}$$

$$\mathbb{D}_{\mathrm{Q}} \in \Im\{\mathbb{D}\} \tag{3.14}$$

where $\mathbb{D}$ is the the J-QAM mapping alphabet.

In order to further clarify the notation used in (3.12), consider the factor graph represented by Figure 3.5.

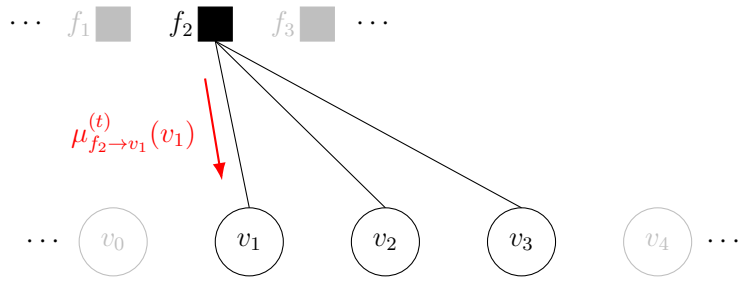

Figure 3.5 – *Example of a factor graph.*

The message from factor node f_2 to variable node v_1 is calculated by summing over all possible values assumed by v_2 and v_3 simultaneously multiplied by previous messages from v_2 and v_3 to f_2, i.e.,

$$\mu^{(t)}_{f_2 \to v_1}(v_1) = \sum_{\sim\{v_2\}} g(v_1, v_2, v_3) \times \prod_{u \in N(f_2)\backslash 1} \mu^{(t-1)}_{v_u \to f_2}(v_u), \tag{3.15}$$

where $g(v_1, v_2, v_3)$ is a function of v_1, v_2 and v_3. The summation in (3.15) is defined as

$$\sum_{\sim\{v_2\}} g(v_1, v_2, v_3) \triangleq \sum_{v_2 \in \mathbb{A}_2} \sum_{v_3 \in \mathbb{A}_3} g(v_1, v_2, v_3), \tag{3.16}$$

where the alphabet of each variable v_i is $\mathbb{A}_i$. In literature, this type of summation is called *summary*, and it indicates the variable that is not being summed over [32].

Messages from variable node $\mathbf{d}^{(j)}$ to factor node f_i over the tth iteration are given by

$$\mu^{(t)}_{\mathbf{d}^{(j)} \to f_i}\left(\mathbf{d}^{(j)}\right) = \prod_{u \in N(\mathbf{d}^{(j)})\backslash i} \mu^{(t-1)}_{f_u \to \mathbf{d}^{(j)}}\left(\mathbf{d}^{(j)}\right), \tag{3.17}$$

where $N(\mathbf{d}^{(j)})\backslash i$ represents the set of factor nodes connected to $\mathbf{d}^{(j)}$ excluding the ith node.

After τ iterations, the non-normalized marginal probability distribution of each data component is given by the multiplication of all incoming messages at

the variable nodes $\mathbf{d}^{(j)}$, yielding to

$$p\left(\mathbf{d}^{(j)}\right) = \prod_{u \in N(\mathbf{d}^{(j)})} \mu^{(\tau)}_{f_u \to \mathbf{d}^{(j)}}\left(\mathbf{d}^{(j)}\right). \tag{3.18}$$

Thus, $p\left(\mathbf{d}^{(j)}\right)$ is the probability mass function that contains the non-normalized likelihood of each possible value assumed by $\mathbf{d}^{(j)}$. Therefore, MAP criterion can be used for estimating the received data components.

Algorithm 1 presents the pseudo code for the receiver considering the graph shown in Figure 3.4.

Algorithm 1 SPA based detection algorithm pseudo code

function SPA_RECEIVER($\mathbf{y}, \mathbf{\Psi}_\mathrm{I}, \mathbf{\Psi}_\mathrm{Q}, \tau$)
  $\mu_{f_i \to \mathbf{d}_\mathrm{I}{}^{(j)}}\left(\mathbf{d}_\mathrm{I}{}^{(j)}\right) = \mathbf{1}$; ▷ Initialize messages from factor to variable nodes
  $\mu_{f_i \to \mathbf{d}_\mathrm{Q}{}^{(j)}}\left(\mathbf{d}_\mathrm{Q}{}^{(j)}\right) = \mathbf{1}$;
  $\mu_{\mathbf{d}_\mathrm{I}{}^{(j)} \to f_i}\left(\mathbf{d}_\mathrm{I}{}^{(j)}\right) = \mathbf{0}$; ▷ Initialize messages from variable to factor nodes
  $\mu_{\mathbf{d}_\mathrm{Q}{}^{(j)} \to f_i}\left(\mathbf{d}_\mathrm{Q}{}^{(j)}\right) = \mathbf{0}$; ▷ All these vectors have $J/2$ elements
  for $t = 1 : \tau$ **do**
    compute $\mu^{(t)}_{f_i \to \mathbf{d}_\mathrm{I}{}^{(j)}}\left(\mathbf{d}_\mathrm{I}{}^{(j)}\right)$ and $\mu^{(t)}_{f_i \to \mathbf{d}_\mathrm{Q}{}^{(j)}}\left(\mathbf{d}_\mathrm{Q}{}^{(j)}\right)$ according with (3.12);
    compute $\mu^{(t)}_{\mathbf{d}_\mathrm{I}{}^{(j)} \to f_i}\left(\mathbf{d}_\mathrm{I}{}^{(j)}\right)$ and $\mu^{(t)}_{\mathbf{d}_\mathrm{Q}{}^{(j)} \to f_i}\left(\mathbf{d}_\mathrm{Q}{}^{(j)}\right)$ according with (3.17);
  end for
  compute $p\left(\mathbf{d}_\mathrm{I}{}^{(j)}\right)$ and $p\left(\mathbf{d}_\mathrm{Q}{}^{(j)}\right)$ according with (3.18);
  Estimated most probable symbol via MAP;
end function

It is important to point out that messages must be calculated for the in-phase and quadrature components, i.e., one algorithm for Figure 3.4 (a) and one for (b). However, this two different algorithms can operate in parallel. This characteristic leads to a less complex algorithm when compared to a possible approach where a single algorithm is used to estimate complex-valued symbols, since the required computational capacity for message computation is directly related to the number of possible values assumed by transmit data symbols.

Considering the graph shown in Figure 3.4, one can see that it is a cyclic graph where the girth of the graph, i.e., its shortest cycle, equals four. As a result, iterative message passing becomes necessary for convergence [32][58]. Although the resulting marginal probabilities will not be exact, numerical simulations show a good match with theoretical bit error probability curves.

At the algorithm first iteration in (3.12), one needs to initialize the messages from variable nodes to factor nodes in order to start the iterative message computation. These messages are preloaded with 1 [59].

A key point of this demodulating approach lies in the fact that estimation of noise variance and equalization prior to demodulation are not necessary for message computation. Only channel state information (CSI) is required. Note that GFDM detection would also be possible following the same approach.

3.3 Chapter Summary

In this chapter, a modification in the GFDM's scheme led to a waveform that performs identically to FBMC-OQAM. Hence, enlarging the set of waveforms that can be derived from GFDM. Using this formulation for FBMC-OQAM a demodulation algorithm based on the SPA was proposed. The next chapter evaluates the behavior of these afore mentioned schemes employing numerical simulations.

Chapter 4

Performance Evaluation

In this chapter the performance of Linear GFDM and of the SPA-based demodulator are evaluated. Numerical simulations using MATLAB® were employed for estimating the performances.

4.1 Linear GFDM Performance Evaluation

This section presents the BER of Linear GFDM, FBMC-OQAM, OFDM and GFDM under three different channel models. The BER curves are compared with OFDM and GFDM theoretical bit error probability curves, which are presented in Appendix A. Later, it presents the waveforms estimated power spectral density (PSD), and the impact on spectral containment when Martin pulse with different overlapping factors is used as prototype filter in Linear GFDM. Last, it presents estimated complementary cumulative distribution function (CCDF) of the peak-to-average power ratio (PAPR).

4.1.1 Bit Error Ratio

Three channel models were used for evaluating the BER: *i*) Additive white Gaussian noise (AWGN); *ii*) Time-invariant frequency-selective (TIFS); and *iii*) Time-variant frequency-selective (TVFS). Table 4.1 shows the channel impulse responses used for the simulations.

The notation $r \sim \mathcal{CN}(0, 1)$ means that r follows a complex normal distribution with zero mean and unitary variance. The TIFS and TVFS channels impulse responses were chosen for the coherence bandwidth to be greater than the subcarrier bandwidth. Therefore, flat fading was assumed per subcarrier and frequency domain equalization was employed.

Table 4.1 – *Channel models I.*

Channel model	Impulse response
AWGN	$\mathbf{h}_{\text{AWGN}} = 1$
Time-invariant frequency-selective	$\mathbf{h}_{\text{TIFS}} = [1\ 0\ 0\ 0.1\ 0\ 0\ 0.01]$
Time-variant frequency-selective	$\mathbf{h}_{\text{TVFS}} = \left[\frac{1}{\sqrt{2}}r_0\ \frac{0}{\sqrt{2}}r_1\ \frac{0.01^2}{\sqrt{2}}r_2\ \frac{0.02^2}{\sqrt{2}}r_3\right]$, where $r_n \sim \mathcal{CN}(0,1)$

Table 4.2 shows the waveforms simulation parameters employed.

Table 4.2 – *Waveform related simulation parameters I.*

Parameter	Linear GFDM	FBMC-OQAM	OFDM	GFDM
Mapping	16-QAM	16-QAM	16-QAM	16-QAM
Prototype filter	Martin	Martin	Rect	Raised cosine
Subcarriers (K)	128	128	384	128
Subsymbols (M)	3	–	1	3
Overlapping factor (Θ)	–	3	–	–
Roll off factor (α)	–	–	–	0.2 and 0.9
Symbols per frame	384	384	384	384

Closed form symbol error probability expressions for GFDM and OFDM under the channel models are presented in Appendix A.

BER results for AWGN channel are shown in Figure 4.1. It is possible to observe that Linear GFDM holds the same performance as OFDM and FBMC-OQAM. This performance is observed since ISI is avoided by the half Nyquist prototype filter and, ICI is avoided with the OQAM configuration. For this reason, the system is considered quasi-orthogonal, and the BER follows the OFDM bit error probability when the CP is not taken into account and a long stream of data is assumed. GFDM shows a performance degradation due to noise enhancement from the zero forcing demodulator. It is valid to note that if GFDM's prototype filter is orthogonal in time and frequency domains ($\alpha = 0$), the BER performance would follow the OFDM bit error probability as well, again, when CP is not taken into account.

Figure 4.2 shows the BER over TIFS channel. The signal-to-noise ratio (SNR) is weighted by the channel's frequency response over the kth subcarrier for all waveforms. Thus, a performance degradation is observed when compared with the AWGN channel. At the receiver, perfect channel estimation is assumed. For performing the channel equalization, frequency domain zero-forcing equalization was employed. As one can see, Linear GFDM holds the same performance as OFDM and FBMC-OQAM. GFDM displays the same performance loss from the AWGN channel due to noise enhancement from the ZF demodulation matrix.

Figure 4.3 presents the performance under TVFS channel. In this scenario, the channel impulse response changes at every multicarrier frame transmission, thus fashioning a time-variant block fading channel. Each subcarrier experiences a flat frequency response since the channel's coherence bandwidth is approximately 20 times larger than the subcarrier bandwidth. As in the last case, channel state information is known by the receiver and the equalization is performed in frequency domain with the zero-forcing solution. Again, the same comments applied to the last two cases are still valid for the TVFS channel.

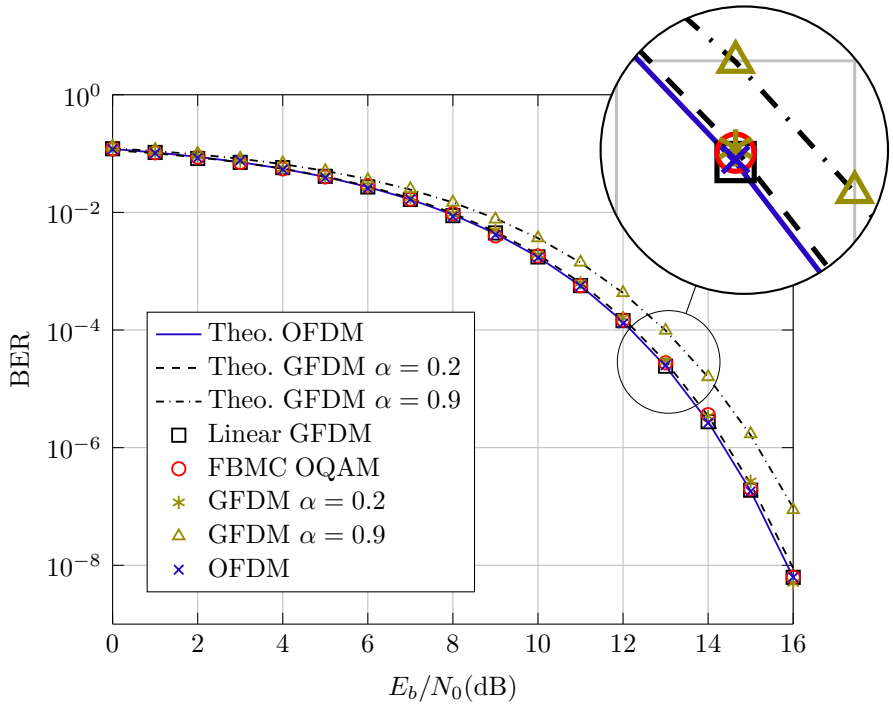

Figure 4.1 – *BER performance from Linear GFDM, FBMC-OQAM, GFDM and OFDM under AWGN channel.*

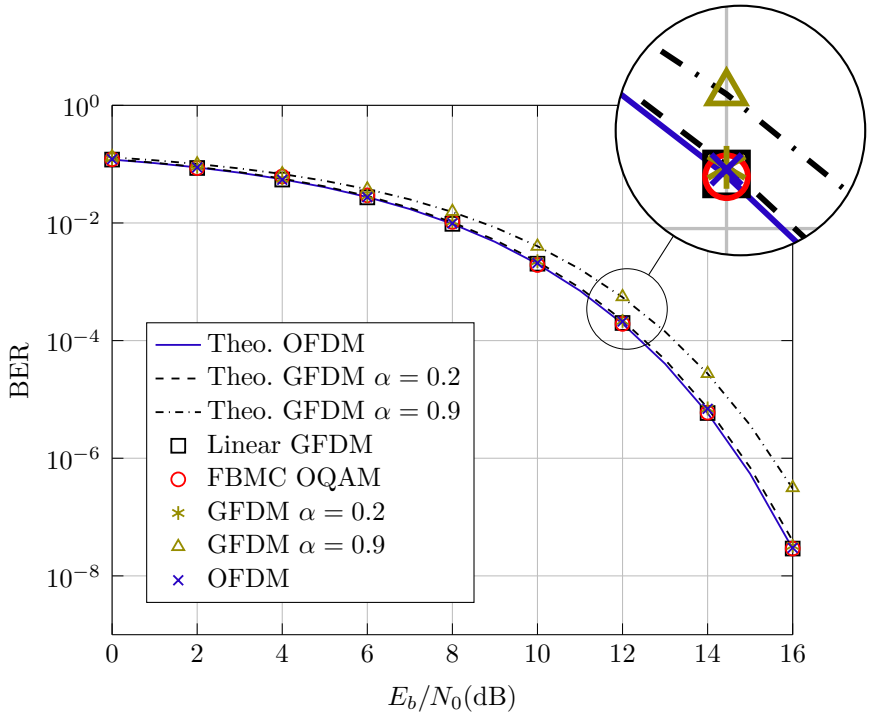

Figure 4.2 – *BER performance from Linear GFDM, FBMC-OQAM, GFDM and OFDM under time-invariant frequency-selective channel.*

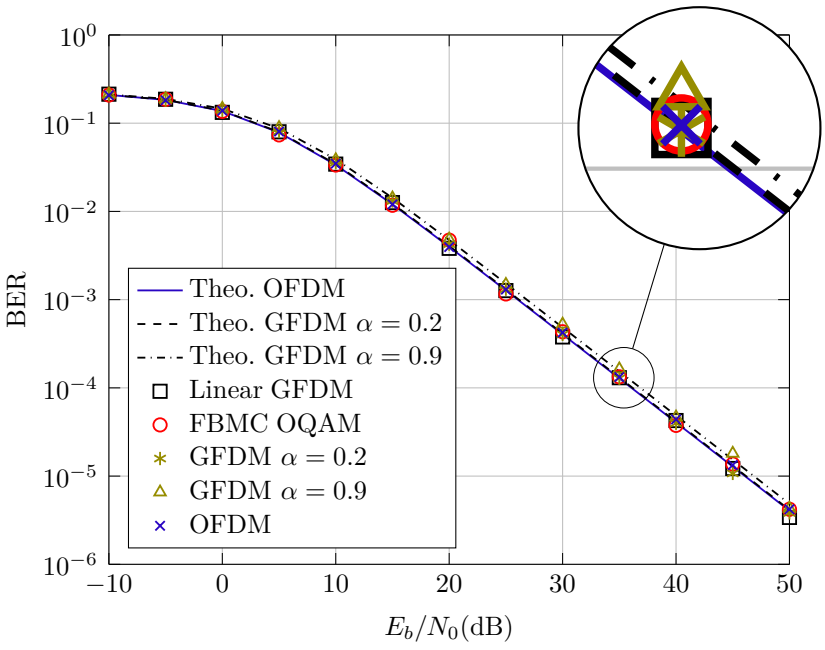

Figure 4.3 – *BER performance from Linear GFDM, FBMC-OQAM, GFDM and OFDM under time-variant frequency-selective channel.*

4.1.2 Spectral Containment

For estimating the PSD, the Welch method [61] was employed using a Blackman-Harris window. Figure 4.4 shows the estimated PSD of Linear GFDM,

FBMC-OQAM, GFDM and OFDM.

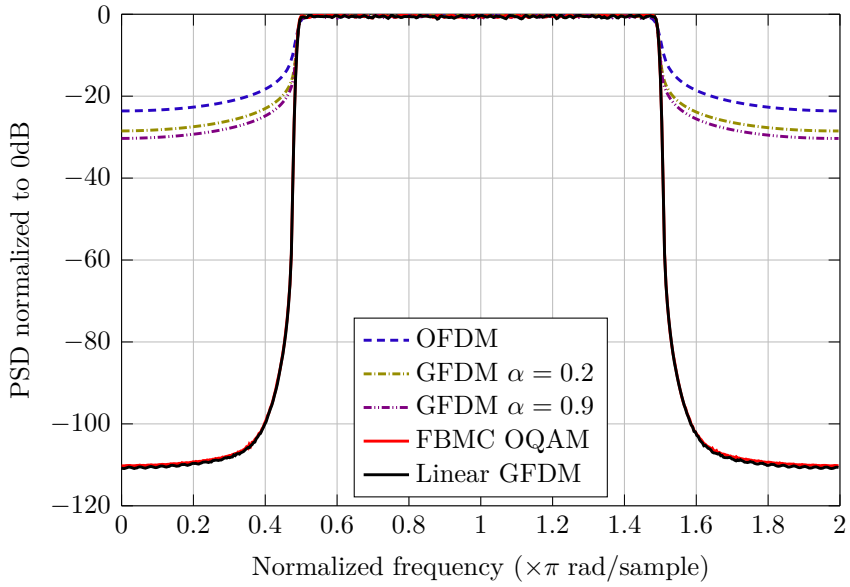

Figure 4.4 – *Estimated PSD from Linear GFDM, FBMC-OQAM, GFDM and OFDM.*

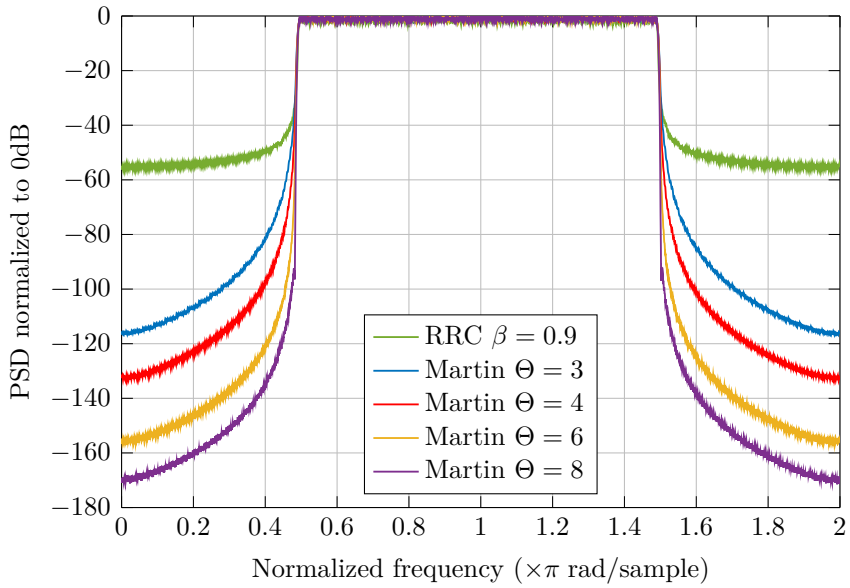

Figure 4.5 – *Estimated PSD from Linear GFDM using different overlapping factors.*

Linear GFDM holds the same PSD as FBMC-OQAM due to the linear filtering behavior of the modified modulation matrices. In addition, the Martin pulse frequency localization allows very low levels of energy leakage outside the signal band. OFDM shows the largest OOB emission due to its *sinc* shaped subcarriers. GFDM shapes subcarriers with a raised cosine (RC) filter. Hence, it presents smaller OOB emission when compared to OFDM due to its prototype

filter localization. However, the circular filtering employed by GFDM leads to discontinuities among frames, which limits lower OOB emissions.

Employing Martin pulse as prototype filter leads to a trade off between spectral containment and the length of the transmit signal. Figure 4.5 shows the PSD of Linear GFDM when different overlapping factors are used. As the number of subsymbols increases, the length of the multicarrier frame also increases. Therefore, smaller OOB emission is achieved. For the sake of comparison, the estimated PSD of Linear GFDM with root raised cosine (RRC) ($\beta = 0.9$) pulse as prototype filter is also shown.

4.1.3 Peak-to-average Power Ratio

This subsection presents the performance of the waveforms in terms of the CCDF of the PAPR. The CCDF shows the estimated probability that the signal's PAPR assumes a value greater than a reference level denoted by $PAPR_0$. The simulation result is shown in Figure 4.6. For estimating the CCDF, a set of 10^6 multicarrier frames were transmitted.

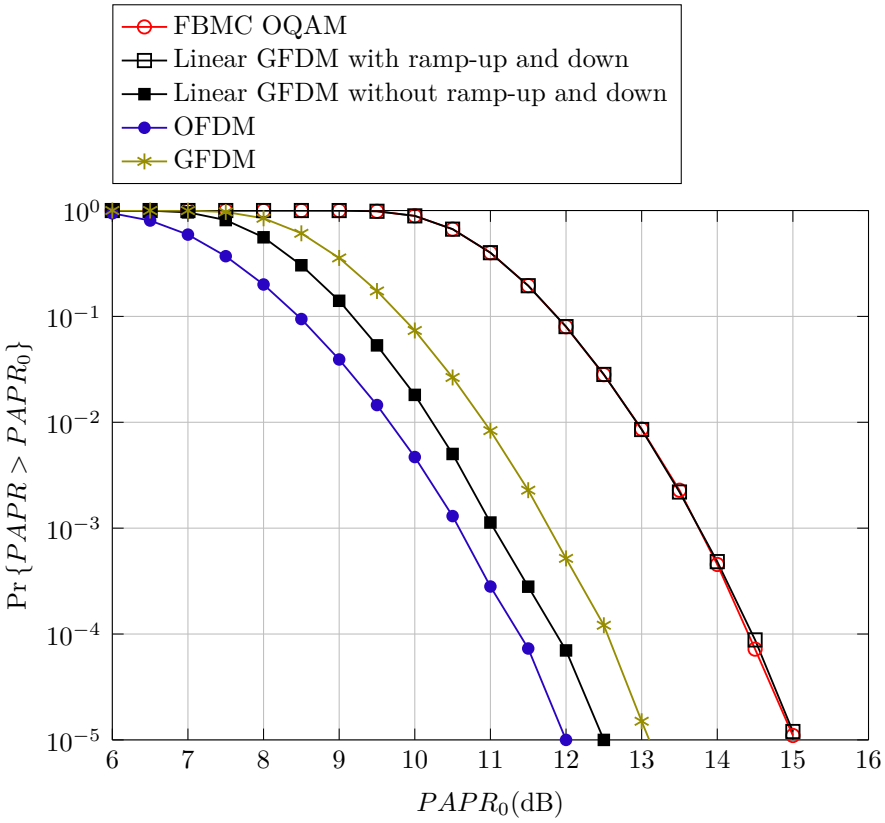

Figure 4.6 – *Estimated CCDF of the PAPR.*

Unfortunately, high levels of PAPR are present in FBMC-OQAM and Linear GFDM due to the ramp-up and ramp-down of the transmit signal. However, considering transmission of a continuous or long stream of data, these ramp-up and ramp-down become negligible, and the Linear GFDM curve comes closer to the OFDM curve as shown in Figure 4.6. Note that the same is true for FBMC.

4.2 SPA Based Demodulator Performance Evaluation

Section 4.2 presents the estimated BER of Linear GFDM under two different channel models, namely AWGN and Rayleigh, employing the SPA based demodulator, which are compared with theoretical OFDM bit error probability curves. Furthermore, an complexity analysis of the algorithm is presented.

4.2.1 Bit Error Ratio

Two channel models were used for evaluating the BER of the SPA based demodulator: *i*) AWGN; and *ii*) Rayleigh. The Rayleigh channel is block fading, in which a new impulse response is draw at every frame transmission.

Table 4.3 describes the channel models used in simulations.

Table 4.3 – *Channel models II.*

Channel model	Impulse response
AWGN	$\mathbf{h}_{\text{AWGN}} = 1$
Rayleigh	$\mathbf{h}_{\text{Rayleigh}} = r$, where $r \sim \mathcal{CN}(0,1)$

Table 4.4 shows the waveforms simulation parameters employed for this Section.

Figure 4.7 shows the resultant BER performance under AWGN considering $\tau = 1$ and $\tau = 7$ iterations. All in all, the algorithm shows a gap when compared with the theoretical OFDM bit error probability. For $\tau = 7$ iterations performance was slightly improved when compared to a single iteration. This performance gap happens due to the cyclic nature of the graph shown in Figure 3.4, i.e., the estimated marginal distributions delivered by the algorithm are not exact. Therefore, this performance loss was expected.

Figure 4.8 shows the resultant BER performance under Rayleigh channel considering $\tau = 1$ and $\tau = 7$ iterations. In this case, the SPA based demodulator

Table 4.4 – *Waveform related simulation parameters II.*

Parameter	Value
Waveform	Linear GFDM
Mapping	4-QAM
Prototype filter	Martin
Subcarriers (K)	2
Subsymbols (M)	3
Data symbols per frame	6
Samples per frame	11
Number of iterations	$\tau = 1$ and $\tau = 7$

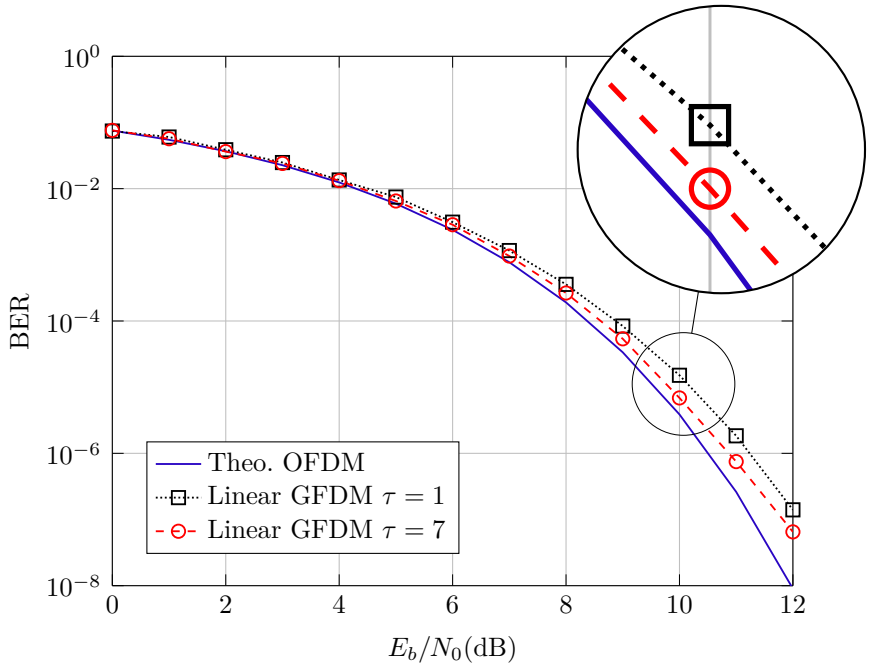

Figure 4.7 – *BER performance from Linear GFDM under AWGN channel employing the SPA based demodulator.*

converges equally to the performance of the theoretical OFDM curve. This performance can be explained with the fact that the equivalent matrices, described in (3.10), are now modified by the random nature of the channel. As a result, the associated edge values, i.e., the samples from $\mathbf{\Psi}$, do not have the same values at each consecutive frame transmission. Therefore, the performance loss expected from the cycles in the graph is not present in this scenario. In essence, this characteristic represents a great advantage over linear demodulation schemes, since it

uses the channel variations in its favor. Moreover, estimation of the noise variance was not necessary, as well as equalization prior to demodulation.

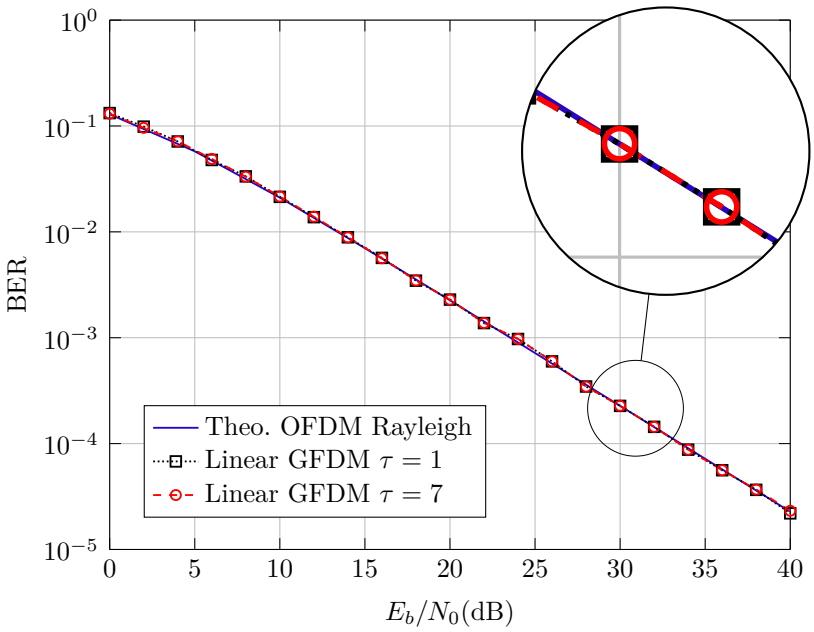

Figure 4.8 – *BER performance from Linear GFDM under Rayleigh channel employing the SPA based demodulator.*

4.2.2 Complexity

In the complexity analysis, we take into account the number of complex multiplications performed for estimating one complex-valued J-QAM data symbol vector whose length is given by $N = KM$. For computing the messages given by (3.12), one needs $N - 1$ *for* loops. These loops' index run from 1 to $J/2$ because real and imaginary parts of the QAM symbol are estimated independently. Taking into consideration that the algorithm performs message calculations iteratively, and adding the computation of messages given by (3.17). The algorithm is built in such manner that the number of complex multiplications required for estimating a QAM data symbol vector with length N is given by

$$\mathcal{C} = \Big[\Big(8N^3 - 4N^2K - 8N^2 + 2NK + 2N\Big)\Big(J/2\Big)^{N-1} + \; 2N^3 - 8N^2 + 6N\Big]\tau. \quad (4.1)$$

Therefore, the complexity required for estimating represents a drawback of the SPA-based algorithm.

4.3 Chapter Summary

In this Chapter, it was shown that Linear GFDM holds the same performance as FBMC-OQAM in terms of quasi-orthogonality, OOB emission and PAPR. Hence, GFDM can be regarded as a flexible waveform scheme that is able to attend different design criteria depending on the foreseen application.

Moreover, the performance evaluation of the SPA based receiver shows that, under the simulation constrains, the receiver algorithm is able to deliver performance comparable to orthogonal schemes without requiring a priori noise variance estimation and channel equalization.

Chapter 5

Conclusion and Future Work

In this dissertation, a study covering the most prominent multicarrier waveforms was carried. Their transceiver design followed by the basic procedure for channel equalization was presented in Chapter 2. Thereafter, Linear GFDM, which presents the same characteristics of FBMC-OQAM, was presented using GFDM's matrix formulation. Consequently, the set of waveforms that can be obtained from GFDM was extended, and scenarios in which low OOB emission is critical can benefit from this GFDM configuration. Furthermore, taking advantage of the separation between real and imaginary parts of the transmit data symbols in Linear GFDM, a reduced complexity demodulation algorithm based on the SPA was formulated for jointly equalize the channel and detect the transmitted data symbols. The performance of the proposed techniques was evaluated through numerical simulations with MATLAB®. As one can see in chapter 4, results are in accordance with theoretical bit error probability curves, as well as with expected performance indications.

All in all, non-orthogonal waveforms show promising characteristics that future wireless systems may take advantage. In particular, the low OOB emission is an advantageous characteristic for CR systems, which may allow the usage of TVWS without causing harmful interference to primary users. Therefore, it may allow, for example, affordable Internet access to rural and remote areas where current wireless standards lack coverage. Waveforms which present low OOB emissions can deliver robustness against time variant channels, since frequency dispersion caused by the Doppler effect leads to loss of orthogonality between subcarriers in multicarrier systems. Hence, the amount of interference that the system is subjected will depend upon the frequency localization of each subcarrier, which is depend on the pulse shaping filter used as prototype. Moreover, IoT applications that require reduced energy consumption can save battery life via

unsynchronized transmissions, since the multiuser interference that would arise from rough synchronized transmissions depends upon the waveform frequency localization. As demonstrated, Linear GFDM may be suitable for communication systems that will operate in conditions where low OOB emission is essential.

While the current non-orthogonal transceiver schemes present rather elevated complexity when compared to OFDM, efforts have been made for designing detection algorithms with affordable complexity. Likewise, borrowing techniques from contexts such as Machine Learning and Neural Networks to obtain detection algorithms that can take full exploitation of what these techniques have to offer are presenting interesting solutions as well as challenging questions.

Future work perspectives point towards iterative detection algorithms that are able to simultaneously estimate and compensate the channel induced distortions as well as interferences that arise from the non-orthogonal nature of the waveforms. Specifically, other instances from the class of MPAs can be employed for achieving such objective in future research.

Bibliography

[1] ANDREWS, J. G. et al. What will 5G be? *IEEE Journal on selected areas in communications*, IEEE, v. 32, n. 6, p. 1065–1082, 2014.

[2] SOLDANI, D.; MANZALINI, A. Horizon 2020 and beyond: On the 5G operating system for a true digital society. *IEEE Vehicular Technology Magazine*, v. 10, n. 1, p. 32–42, March 2015. ISSN 1556-6072.

[3] DAHLMAN, E. et al. 5G radio access. *Ericsson review*, v. 6, p. 2–7, 2014.

[4] DAWY, Z. et al. Toward massive machine type cellular communications. *IEEE Wireless Communications*, v. 24, n. 1, p. 120–128, February 2017. ISSN 1536-1284.

[5] FETTWEIS, G.; ALAMOUTI, S. 5G: Personal mobile internet beyond what cellular did to telephony. *IEEE Communications Magazine*, v. 52, n. 2, p. 140–145, February 2014. ISSN 0163-6804.

[6] International Telecomunications Union. Recommendation ITU-R M.2083-0, *IMT Vision – Framework and overall objectives of the future development of IMT for 2020 and beyond*. Accessed: 02/27/2018. Disponível em: <http://www.itu.int/dms_pubrec/itu-r/rec/m/R-REC-M.2083-0-201509-I!!PDF-E.pdf>.

[7] OSSEIRAN, A. et al. Scenarios for 5G mobile and wireless communications: the vision of the METIS project. *IEEE Communications Magazine*, IEEE, v. 52, n. 5, p. 26–35, 2014.

[8] NIU, Y. et al. A survey of millimeter wave communications (mmWave) for 5G: opportunities and challenges. *Wireless Networks*, v. 21, n. 8, p. 2657–2676, Nov 2015. ISSN 1572-8196. Disponível em: <https://doi.org/10.1007/s11276-015-0942-z>.

[9] AGIWAL, M.; ROY, A.; SAXENA, N. Next generation 5G wireless networks: A comprehensive survey. *IEEE Communications Surveys Tutorials*, v. 18, n. 3, p. 1617–1655, thirdquarter 2016. ISSN 1553-877X.

[10] KUNDARGI, N. *5G Standardization 3GPP Status Update and Overview*. Accessed: 04/06/2018. Disponível em: <ftp://ftp.ni.com/pub/branches/japan/ekit/3gpp_resource_guide_2017.pdf>.

[11] MA, Z. et al. Key techniques for 5G wireless communications: network architecture, physical layer, and MAC layer perspectives. *Science China information sciences*, Springer, v. 58, n. 4, p. 1–20, 2015.

[12] Ericsson. White paper, *5G Systems – Enabling the Transformation of Industry and Society*. Accessed: 03/06/2018. Disponível em: <https://www.ericsson.com/assets/local/publications/white-papers/wp-5g-systems.pdf>.

[13] ZHANG, S. et al. 5G: Towards energy-efficient, low-latency and high-reliable communications networks. In: *2014 IEEE International Conference on Communication Systems*. [S.l.: s.n.], 2014. p. 197–201.

[14] ATZORI, L.; IERA, A.; MORABITO, G. The internet of things: A survey. *Computer networks*, Elsevier, v. 54, n. 15, p. 2787–2805, 2010.

[15] Ericsson. White paper, *5G Radio Access – Capabilities and Technologies*. Accessed: 03/06/2018. Disponível em: <https://www.ericsson.com/assets/local/publications/white-papers/wp-5g.pdf>.

[16] PALATTELLA, M. R. et al. Internet of things in the 5G era: Enablers, architecture, and business models. *IEEE Journal on Selected Areas in Communications*, v. 34, n. 3, p. 510–527, March 2016. ISSN 0733-8716.

[17] SETHI, P.; SARANGI, S. R. Internet of things: architectures, protocols, and applications. *Journal of Electrical and Computer Engineering*, Hindawi, 2017.

[18] FARHANG-BOROUJENY, B.; KEMPTER, R. Multicarrier communication techniques for spectrum sensing and communication in cognitive radios. *IEEE Communications Magazine*, v. 46, n. 4, p. 80–85, April 2008. ISSN 0163-6804.

[19] MURARA, B. *IMT–2020 Network High Level Requirements, How African Countries can Cope*. Accessed: 03/06/2018. Disponível em: <https://www.itu.int/en/ITU-T/Workshops-and-Seminars/standardization/20170402/Documents/S2_4.%20Presentation_IMT%202020%20Requirements-how%20developing%20countries%20can%20cope.pdf>.

[20] WUNDER, G. et al. 5GNOW: non-orthogonal, asynchronous waveforms for future mobile applications. *IEEE Communications Magazine*, v. 52, n. 2, p. 97–105, February 2014. ISSN 0163-6804.

[21] GERZAGUET, R. et al. The 5G candidate waveform race: a comparison of complexity and performance. *EURASIP Journal on Wireless Communications and Networking*, v. 2017, n. 1, p. 13, Jan 2017. ISSN 1687-1499. Disponível em: <https://doi.org/10.1186/s13638-016-0792-0>.

[22] EECKHAUTE, M. V. et al. Performance of emerging multi-carrier waveforms for 5G asynchronous communications. *EURASIP Journal on Wireless Communications and Networking*, v. 2017, n. 1, p. 29, Feb 2017. ISSN 1687-1499. Disponível em: <https://doi.org/10.1186/s13638-017-0812-8>.

[23] ZHANG, D. et al. A study on the link level performance of advanced multicarrier waveforms under mimo wireless communication channels. *IEEE Transactions on Wireless Communications*, v. 16, n. 4, p. 2350–2365, April 2017. ISSN 1536-1276.

[24] BELLANGER, M. Physical layer for future broadband radio systems. In: *2010 IEEE Radio and Wireless Symposium (RWS)*. [S.l.: s.n.], 2010. p. 436–439. ISSN 2164-2958.

[25] STITZ, T. H. Filterbank techniques for the physical layer in wireless communications. *Tampereen teknillinen yliopisto. Julkaisu-Tampere University of Technology. Publication; 919*, 2010.

[26] FARHANG-BOROUJENY, B. Filter bank multicarrier modulation: A waveform candidate for 5G and beyond. *Advances in Electrical Engineering*, Hindawi, v. 2014, 2014.

[27] RENFORS, M. et al. Filter banks for next generation multicarrier wireless communications. *EURASIP Journal on Advances in Signal Processing*, v. 2010, n. 1, p. 314193, May 2010. ISSN 1687-6180. Disponível em: <http://downloads.hindawi.com/journals/specialissues/328295.pdf>.

[28] MICHAILOW, N. et al. Generalized frequency division multiplexing for 5th generation cellular networks. *IEEE Transactions on Communications*, v. 62, n. 9, p. 3045–3061, Sept 2014. ISSN 0090-6778.

[29] FETTWEIS, G.; KRONDORF, M.; BITTNER, S. GFDM - generalized frequency division multiplexing. In: *VTC Spring 2009 - IEEE 69th Vehicular Technology Conference*. [S.l.: s.n.], 2009. p. 1–4. ISSN 1550-2252.

[30] GASPAR, I. et al. GFDM–A framework for virtual PHY services in 5G networks. *arXiv preprint arXiv:1507.04608*, 2015.

[31] GALLAGER, R. Low-density parity-check codes. *IRE Transactions on information theory*, IEEE, v. 8, n. 1, p. 21–28, 1962.

[32] KSCHISCHANG, F. R.; FREY, B. J.; LOELIGER, H. A. Factor graphs and the sum-product algorithm. *IEEE Transactions on Information Theory*, v. 47, n. 2, p. 498–519, Feb 2001. ISSN 0018-9448.

[33] KAYNAK, M. N.; DUMAN, T. M.; KURTAS, E. M. Belief propagation over frequency selective fading channels. In: *IEEE 60th Vehicular Technology Conference, 2004. VTC2004-Fall. 2004.* [S.l.: s.n.], 2004. v. 2, p. 1367–1371 Vol. 2. ISSN 1090-3038.

[34] RAVITEJA, P. et al. Low-complexity iterative detection for orthogonal time frequency space modulation. In: IEEE. *2018 IEEE Wireless Communications and Networking Conference (WCNC)*. [S.l.], 2018. p. 1–6.

[35] ZHANG, D. et al. Expectation propagation for near-optimum detection of mimo-gfdm signals. *IEEE Transactions on Wireless Communications*, v. 15, n. 2, p. 1045–1062, Feb 2016. ISSN 1536-1276.

[36] WU, S. et al. Expectation propagation approach to joint channel estimation and decoding for ofdm systems. In: *2014 IEEE International Conference on Acoustics, Speech and Signal Processing (ICASSP)*. [S.l.: s.n.], 2014. p. 1941–1945. ISSN 1520-6149.

[37] SEXTON, C. et al. Enabling asynchronous machine-type D2D communication using multiple waveforms in 5G. *IEEE Internet of Things Journal*, PP, n. 99, p. 1–1, 2018.

[38] BANELLI, P. et al. Modulation formats and waveforms for 5G networks: Who will be the heir of OFDM?: An overview of alternative modulation schemes for improved spectral efficiency. *IEEE Signal Processing Magazine*, v. 31, n. 6, p. 80–93, Nov 2014. ISSN 1053-5888.

[39] NISSEL, R.; SCHWARZ, S.; RUPP, M. Filter bank multicarrier modulation schemes for future mobile communications. *IEEE Journal on Selected Areas in Communications*, v. 35, n. 8, p. 1768–1782, Aug 2017. ISSN 0733-8716.

[40] KOREVAAR, C. W. et al. Spectrum efficient, localized, orthogonal waveforms: Closing the gap with the Balian-Low theorem. *IEEE Transactions on Communications*, v. 64, n. 5, p. 2155–2165, May 2016. ISSN 0090-6778.

[41] HWANG, T. et al. OFDM and its wireless applications: A survey. *IEEE Transactions on Vehicular Technology*, v. 58, n. 4, p. 1673–1694, May 2009. ISSN 0018-9545.

[42] FARHANG-BOROUJENY, B. OFDM versus filter bank multicarrier. *IEEE Signal Processing Magazine*, v. 28, n. 3, p. 92–112, May 2011. ISSN 1053-5888.

[43] CHANG, R. High-speed multichannel data transmission with bandlimited orthogonal signals. *Bell Sys. Tech. J*, v. 45, n. 10, p. 1775–1796, 1966.

[44] SALTZBERG, B. Performance of an efficient parallel data transmission system. *IEEE Transactions on Communication Technology*, v. 15, n. 6, p. 805–811, December 1967. ISSN 0018-9332.

[45] CHERUBINI, G.; ELEFTHERIOU, E.; OLCER, S. Filtered multitone modulation for very high-speed digital subscriber lines. *IEEE Journal on Selected Areas in Communications*, v. 20, n. 5, p. 1016–1028, Jun 2002. ISSN 0733-8716.

[46] WANG, T.; PROAKIS, J. G.; ZEIDLER, J. R. Interference analysis of filtered multitone modulation over time-varying frequency-selective fading channels. *IEEE Transactions on Communications*, v. 55, n. 4, p. 717–727, April 2007. ISSN 0090-6778.

[47] FARHANG-BOROUJENY, B.; YUEN, C. H. Cosine modulated and offset QAM filter bank multicarrier techniques: A continuous-time prospect. *EURASIP Journal on Advances in Signal Processing*, Hindawi Publishing Corp., New York, NY, United States, v. 2010, p. 6:1–6:11, jan. 2010. ISSN 1110-8657. Disponível em: <http://dx.doi.org/10.1155/2010/165654>.

[48] MARTIN, K. W. Small side-lobe filter design for multitone data-communication applications. *IEEE Transactions on Circuits and Systems II: Analog and Digital Signal Processing*, v. 45, n. 8, p. 1155–1161, Aug 1998. ISSN 1057-7130.

[49] VIHOLAINEN, A.; BELLANGER, M.; HUCHARD, M. Deliverable 5.1: Prototype filter and structure optimization. *Technical Report*, January 2009.

[50] BELLANGER, M. G. Specification and design of a prototype filter for filter bank based multicarrier transmission. In: *2001 IEEE International Conference on Acoustics, Speech, and Signal Processing. Proceedings (Cat. No.01CH37221)*. [S.l.: s.n.], 2001. v. 4, p. 2417–2420 vol.4. ISSN 1520-6149.

[51] MENDES, L. et al. GFDM: providing flexibility for the 5G physical layer. *Opportunities in 5G Networks: A Research and Development Perspective*, CRC Press, p. 325, 2016.

[52] MATTHÉ, M.; MENDES, L. L.; FETTWEIS, G. Generalized frequency division multiplexing in a gabor transform setting. *IEEE Communications Letters*, v. 18, n. 8, p. 1379–1382, Aug 2014. ISSN 1089-7798.

[53] NIMR, A. et al. Optimal radix-2 FFT compatible filters for GFDM. *IEEE Communications Letters*, v. 21, n. 7, p. 1497–1500, July 2017. ISSN 1089-7798.

[54] MICHAILOW, N.; FETTWEIS, G. Low peak-to-average power ratio for next generation cellular systems with generalized frequency division multiplexing. In: *2013 International Symposium on Intelligent Signal Processing and Communication Systems*. [S.l.: s.n.], 2013. p. 651–655.

[55] SEXTON, C. et al. Enabling asynchronous machine-type d2d communication using multiple waveforms in 5g. *IEEE Internet of Things Journal*, v. 5, n. 2, p. 1307–1322, April 2018.

[56] GASPAR, I. et al. Frequency-shift offset-QAM for GFDM. *IEEE Communications Letters*, v. 19, n. 8, p. 1454–1457, Aug 2015. ISSN 1089-7798.

[57] CHO, Y. S. et al. *MIMO-OFDM wireless communications with MATLAB*. [S.l.]: John Wiley & Sons, 2010.

[58] BISHOP, C. M. *Pattern Recognition and Machine Learning*. [S.l.]: Springer, 2006.

[59] LOELIGER, H.-A. An introduction to factor graphs. *IEEE Signal Processing Magazine*, v. 21, n. 1, p. 28–41, Jan 2004. ISSN 1053-5888.

[60] AHMAD, A.; SERPEDIN, E.; QARAQE, K. *Factor graphs and message passing algorithms*. [S.l.]: CRC Press, Boca Raton, FL, 2012.

[61] WELCH, P. The use of fast Fourier transform for the estimation of power spectra: A method based on time averaging over short, modified periodograms. *IEEE Transactions on Audio and Electroacoustics*, v. 15, n. 2, p. 70–73, Jun 1967. ISSN 0018-9278.

[62] SIMON, M. K.; ALOUINI, M.-S. *Digital communication over fading channels*. [S.l.]: John Wiley & Sons, 2005. v. 95.

[63] MENDES, L. L.; MATTHÉ, M. Analysis of symbol error probability equations for OFDM and GFDM. *Unpublished*.

Appendix A

Theoretical Symbol Error Probability Expressions

A.1 OFDM Symbol Error Probability

A.1.1 SEP over AWGN channel

The exact expression for the OFDM symbol error probability (SEP) over AWGN channel is given by

$$p_e = 2\left(\frac{\sqrt{J}-1}{\sqrt{J}}\right)\operatorname{erfc}\left(\sqrt{\gamma}\right) - \left(\frac{\sqrt{J}-1}{\sqrt{J}}\right)^2 \operatorname{erfc}^2\left(\sqrt{\gamma}\right), \tag{A.1}$$

where γ represents the signal-to-noise ratio (SNR) and it is given by

$$\gamma = \frac{3}{2(J-1)}\frac{J}{\log_2(J)}\frac{E_b}{N_0}, \tag{A.2}$$

where N_0 represents the thermal noise power spectral density, E_b the average energy per bit, J the number of symbols in the J-QAM mapping and $\operatorname{erfc}(\cdot)$ represents the complementary error function [62][63].

A.1.2 SEP over frequency-selective channel

Assuming that the channel coherence bandwidth is larger than the bandwidth of one OFDM subcarrier, the exact SEP is given by

$$p_e = \frac{2}{K}\left(\frac{\sqrt{J}-1}{\sqrt{J}}\right)\sum_{k=0}^{K-1}\operatorname{erfc}\left(\sqrt{\gamma(k)}\right) - \frac{1}{K}\left(\frac{\sqrt{J}-1}{\sqrt{J}}\right)^2\sum_{k=0}^{K-1}\operatorname{erfc}^2\left(\sqrt{\gamma(k)}\right), \tag{A.3}$$

where $\gamma(k)$ represents the SNR over the kth subcarrier, and it is given by

$$\gamma(k) = \frac{3}{2(J-1)} \frac{J}{\log_2(J)} \frac{E_b}{N_0} \left|H(k)\right|^2, \tag{A.4}$$

where $H(k)$ denotes the channel frequency response in the kth subcarrier [62][63].

A.1.3 SEP over time-variant frequency-selective channel

Assuming that the channel coherence bandwidth is larger than the bandwidth of one OFDM subcarrier, the exact SEP is given by

$$p_e = \frac{2}{K}\left(\frac{\sqrt{J}-1}{\sqrt{J}}\right)\sum_{k=0}^{K-1}\left(1-\sqrt{\frac{\gamma_r(k)}{1+\gamma_r(k)}}\right) - \frac{1}{K}\left(\frac{\sqrt{J}-1}{\sqrt{J}}\right)^2 \times \left\{\sum_{k=0}^{K-1}\left[1-\frac{4}{\pi}\sqrt{\frac{\gamma_r(k)}{1+\gamma_r(k)}}\arctan\left(\sqrt{\frac{1+\gamma_r(k)}{\gamma_r(k)}}\right)\right]\right\} \tag{A.5}$$

where

$$\gamma_r(k) = \frac{3\sigma_r^2}{J-1} \frac{J}{\log_2(J)} \frac{E_b}{N_0} \left|H(k)\right|^2, \tag{A.6}$$

and σ_r^2 denotes the variance of the complex Gaussian random variable used to obtain the Rayleigh random variable that composes each tap of the channel's impulse response [51][62][63].

A.2 GFDM Symbol Error Probability

A.2.1 SEP over AWGN Channel

Closed form expressions available for the zero forcing demodulation matrix were used. Hence, the GFDM SEP depends upon the ZF demodulation matrix. In this case, intrinsic ISI and ICI from the prototype filter are removed, however a noise enhancement effect arises due to the non-contained frequency response of the demodulation matrix [51][63]. The noise enhancement factor is given by

$$\xi = \sum_{n=0}^{MK-1} \left|\phi_{\mathrm{ZF}}[n]\right|^2, \tag{A.7}$$

where $\phi_{\mathrm{ZF}}[n]$ represents the first row from the demodulation matrix $\mathbf{B}_{\mathrm{ZF}}$.

The SEP is given by

$$p_e = 2\left(\frac{\sqrt{J}-1}{\sqrt{J}}\right)\mathrm{erfc}\left(\sqrt{\varrho}\right) - \left(\frac{\sqrt{J}-1}{\sqrt{J}}\right)^2 \mathrm{erfc}^2\left(\sqrt{\varrho}\right), \tag{A.8}$$

where ϱ is given by

$$\varrho = \frac{3}{2(J-1)} \frac{J}{\log_2(J)} \frac{E_b}{\xi N_0}. \tag{A.9}$$

A.2.2 SEP over frequency-selective channel

Assuming transmission over a time-invariant frequency selective channel, the approximated SEP for the zero forcing demodulation matrix is given by

$$p_e = \frac{2}{K}\left(\frac{\sqrt{J}-1}{\sqrt{J}}\right)\sum_{k=0}^{K-1}\operatorname{erfc}\left(\sqrt{\varrho(k)}\right) - \frac{1}{K}\left(\frac{\sqrt{J}-1}{\sqrt{J}}\right)^2\sum_{k=0}^{K-1}\operatorname{erfc}^2\left(\sqrt{\varrho(k)}\right), \quad \text{(A.10)}$$

where the SNR over the kth subcarrier is represented by

$$\varrho(k) = \frac{3}{2(J-1)}\frac{J}{\log_2(J)}\frac{E_b}{\xi(k)^2 N_0}. \quad \text{(A.11)}$$

The noise enhancement factor for kth subcarrier is given by

$$\xi(k)^2 = \frac{1}{MK}\sum_{l=0}^{MK-1}\left|\frac{\Phi_k[-l]}{H(l)}\right|^2. \quad \text{(A.12)}$$

where $\Phi_k(l)$ represents the frequency response of $\phi_{\mathrm{ZF}}[n]$ over the kth subcarrier [51][63].

A.2.3 SEP over time-variant frequency-selective channel

Assuming that the channel coherence bandwidth is larger than the bandwidth of one GFDM subcarrier and that the channel impulse response remains static during the transmission of one GFDM frame, the approximated SEP for the zero forcing demodulation matrix under time-variant frequency-selective channel is given by

$$p_e = \frac{2}{K}\left(\frac{\sqrt{J}-1}{\sqrt{J}}\right)\sum_{k=0}^{K-1}\left(1-\sqrt{\frac{\varrho_r(k)}{1+\varrho_r(k)}}\right) - \frac{1}{K}\left(\frac{\sqrt{J}-1}{\sqrt{J}}\right)^2 \times \left\{\sum_{k=0}^{K-1}\left[1-\frac{4}{\pi}\sqrt{\frac{\varrho_r(k)}{1+\varrho_r(k)}}\arctan\left(\sqrt{\frac{1+\varrho_r(k)}{\varrho_r(k)}}\right)\right]\right\} \quad \text{(A.13)}$$

where

$$\varrho_r(k) = \frac{3\sigma_r^2}{2(J-1)}\frac{J}{\log_2(J)}\frac{E_b}{\xi(k)^2 N_0}. \quad \text{(A.14)}$$